

Surface Brightness Fluctuation spectra to constrain stellar population properties

A. Vazdekis^{1,2★}, M. Cerviño³, M. Montes⁴, I. Martín-Navarro^{1,2,5,6},
M. A. Beasley^{1,2}

¹*Instituto de Astrofísica de Canarias (IAC), E-38200 La Laguna, Tenerife, Spain*

²*Departamento de Astrofísica, Universidad de La Laguna, E-38205, Tenerife, Spain*

³*Centro de Astrobiología (CSIC/INTA), ESAC Campus, Camino Bajo del Castillo s/n, E-28692 Villanueva de la Cañada, Spain*

⁴*School of Physics, University of New South Wales, Sydney, NSW 2052, Australia*

⁵*Max-Planck Institut für Astronomie, Königstuhl 17, D-69117 Heidelberg, Germany*

⁶*University of California Santa Cruz, 1156 High Street, Santa Cruz, CA 95064, USA*

ABSTRACT

We present a new set of Surface Brightness Fluctuation spectra computed with the E-MILES stellar population synthesis models. The model SBF spectra cover the range $\lambda\lambda$ 1680–50000 Å at moderately high resolution, all based on extensive empirical stellar libraries. The models span the metallicity range $-2.3 \leq [\text{M}/\text{H}] \leq +0.26$ for a suite of IMF types with varying slopes. These predictions can complement and aid fluctuation magnitudes studies, permitting a first order approximation by applying filter responses to the SBF spectra to obtain spectroscopic SBF magnitudes. We provide a recipe for obtaining the latter and discuss their uncertainties and limitations. We compare our spectroscopic SBF magnitudes to photometric data of a sample of early-type galaxies. We also show that the SBF spectra can be very useful for constraining relevant stellar population parameters. We find small ($< 5\%$) mass-fractions of extremely metal-poor components ($[\text{M}/\text{H}] < -1$) on the top of the dominant, old and metal-rich stellar population. These results put stringent constraints on the early stages of galaxy formation in massive elliptical galaxies. This is remarkable given the high degree of degeneracy of the standard spectral analysis to such metal-poor stellar populations in the visible and in the near-IR. The new SBF models show great potential for exploiting ongoing surveys, particularly those based on narrow-band filters.

Key words: galaxies: abundances – galaxies: elliptical and lenticular, cD – galaxies: stellar content – globular clusters: general

1 INTRODUCTION

Surface Brightness Fluctuations (SBFs) were first introduced by [Tonry & Schneider \(1988\)](#) and [Tonry et al. \(1990\)](#) as a way to measure extragalactic distances. These fluctuations are the result of differences in the luminosity distribution of stars that contribute to the flux in each resolution element(s). The SBF is defined as the variance of these fluctuations, normalized to the mean flux of the galaxy in each resolution element. The latter is determined locally as the mean of nearby elements and might require subtracting a smooth galaxy model. Given its connection with the stellar content, a purely theoretical stellar population SBF can be defined as the ratio between the second (variance) and

first (mean) moments of the stellar luminosity function that would be obtained for a stellar population. The resultant SBF is an intrinsic property of the stellar population, intimately related to its evolutionary status. Note that on the top of this signal, there is also a small contribution (less than 0.1%) of Poissonian statistics on the number of stars in different resolution elements ([Cerviño et al. 2008](#)) and, therefore, the SBFs are virtually independent on the amount of stars in the system.

The observational methodology proposed to derive SBF magnitudes ([Tonry & Schneider 1988](#)) requires high quality photometric data. The Fourier Transform (FT) analysis is commonly applied in order to disentangle different signal contaminations. The FT one to obtain accurate local means by disentangling the Point Spread Function (PSF), correlated population variances and the PSF-uncorrelated noise

★ E-mail: vazdekis@iac.es

variance due the observational data acquisition and data processing. In addition it is also a requirement that each resolution element contains a large enough number of stars (at least a few tens of giants [Tonry & Schneider 1988](#)) to avoid statistical biases in the determination of the corresponding moments¹. The fact that the I band fluctuation magnitude for old and metal rich stellar populations depends on the galaxy colour with a small scatter has made the SBF technique a popular secondary distance calibrator (e.g., [Jacoby et al. 1992](#)). In fact SBFs provide robust empirical distance calibrations, such as those of [Blakeslee et al. \(2010\)](#) and [Cantiello et al. \(2018\)](#).

The comparison of theoretical SBF predictions with integrated fluctuation magnitudes and colours is potentially able to provide additional constraints on stellar populations (e.g., [Worthey 1994](#)). It has been shown that the use of the SBFs is able to break the age-metallicity degeneracy affecting old stellar populations ([Worthey 1994](#); [Cantiello et al. 2003](#)). Their relatively modest development can be attributed to a great extent to the difficulties in obtaining SBF magnitudes in more than a single band for the same galaxy. However, there are examples in the literature that have made use of SBF magnitudes and colours and integrated colours to study the stellar populations via comparison with model predictions (e.g., [Blakeslee et al. 2001](#); [Cantiello et al. 2007, 2011](#); [Jensen et al. 2001, 2003](#); [Liu et al. 2000, 2002](#)), including galaxy stellar population gradients (e.g., [Cantiello et al. 2005](#); [Jensen et al. 2015](#)). Such analyses have also been performed in globular clusters (e.g., [Marín-Franch & Aparicio 2006](#)), including the relation between stellar evolutionary modelling and SBF predictions in the Magellanic Clouds ([González, Liu & Bruzual 2004](#); [Mouhcine, González & Liu 2005](#); [Raimondo 2009](#)).

Near-IR SBFs have also been used to constrain the properties of stellar populations ([Liu et al. 2000](#); [González et al. 2004](#)) and to test different mass-loss rates affecting the evolution of Thermally Pulsing Asymptotic Giant Branch (TP-AGB) stars. In fact, [Raimondo et al. \(2005\)](#) showed that NIR SBFs can be used to disentangle observable properties of TP-AGBs. This is particularly relevant for galaxies that contain significant fractions of stellar populations of intermediate ages, which are heavily contributed by these stars. Given the strong connection between the integrated light and its stars, SBFs have been used to test the impact of stellar winds in the evolution of AGB and TP-AGB stars taking advantage of the large sensitivity of the SBFs to these stars, particularly in the IR spectral range ([González-Lópezlira et al. 2010](#); [González-Lópezlira 2018](#)). Moreover, SBFs have been also used to determine the faint end of the galaxy number counts in the Hubble Deep Field-North, extending it by 2 mag beyond the limits of photometric studies ([Marín-Franch & Aparicio 2003](#)).

Despite the fact that most SBF studies have been performed at the photometric level, the method can be also used

in spectroscopy. [Buzzoni \(1993\)](#) modeled the first low resolution SBF spectrum (see their Figure 1). These models, as well as their predictions shown in [Buzzoni \(1989\)](#), are tabulated in terms of their effective number of stars, \mathcal{N}^2 . The SBF spectrum has shown its ability to break stellar population degeneracies by employing particular spectral features in high resolution spectra (see, e.g., [Buzzoni 2005](#), their Fig. 9 and related discussion). Additional SBF spectra, again tabulated as \mathcal{N} , were provided by [González Delgado et al. \(2005\)](#) and presented in [Cerviño & Luridiana \(2009\)](#) and [Cerviño \(2013\)](#) within the context of metric fitting for stellar population studies.

The first observational SBF spectrum of a galaxy was recently presented in [Mitzkus et al. \(2018\)](#). These authors employed the FT analysis as proposed by [Tonry & Schneider \(1988\)](#) to obtain the SBF spectrum of a nearby S0 galaxy, NGC 5102, using data from MUSE Integral Field Spectroscopic (IFS) instrument. These authors also computed model SBF spectra to compare their derived SBF spectrum. They found that including the SBF spectra in the analysis lead to additional constraints in relevant stellar population parameters. Although the pioneering work of these authors has opened a possible way to use IFS data to obtain SBF galaxy spectra, the methodology is currently in its infancy and new investigations are badly needed.

SBF spectral models provide the possibility to derive robust distance estimates, measure SBF magnitudes and constrain stellar populations in galaxies. Moreover, formally, the SBF spectrum should not be restricted necessarily to a particular object, but the method could be extended to any galaxy spectral sample where a common mean and a variance can be estimated.

Here we present new model SBF spectra at moderately high resolution covering a wide range of ages, metallicities and varying IMFs. The main model ingredients are described in Section 2 while the computational details are provided in Section 3. The latter also includes a description of the coverage and behaviour of these models as a function of relevant stellar population parameters. Section 4 provides useful details on how the newly computed SBF spectra can be used for several applications. We compare these new SBF spectra with those predicted by other authors in the literature in Section 5. Finally, we show potential useful applications of these models in Section 6 and summarize our results in Section 7.

2 MODEL INGREDIENTS

2.1 Isochrones

We employ two sets of solar-scaled theoretical isochrones of [Girardi et al. \(2000\)](#) (hereafter Padova00) and [Pietrinferni et al. \(2004\)](#) (hereafter BaSTI). The Padova00 isochrones cover a wide range of ages, from 0.063 to 17.8 Gyr, and six metallicity bins, where $Z = 0.019$ represents the solar value. The range of initial stellar masses extends from 0.15

¹ We note that the requirement of having a few tens of giant stars is equivalent to have the resolution element populated by, at least, several thousands of stars, leading to gaussian distributions of integrated luminosities ([Cerviño & Luridiana 2006](#); [Cerviño et al. 2008](#)). Put in other words, in terms of SBF inferences it implies no correlation between the mean and the variance.

² \mathcal{N} is defined as the ratio between the square of the mean over the variance of the stellar luminosity distribution. Therefore the product of \mathcal{N} and SBF gives the total flux (see [Buzzoni 1989](#) and [Buzzoni 1993](#) Sect. 5)

to $7 M_{\odot}$. A helium fraction was adopted according to the relation: $Y \approx 0.23 + 2.25Z$. The empirical relation by Reimers (1977) is adopted for the mass-loss rates, multiplied by a parameter η that is set to 0.4 (Renzini & Fusi Pecci 1988).

The BaSTI theoretical isochrones of Pietrinferni et al. (2004) were extended as described in Vazdekis et al. (2015), including an extra (supersolar) metallicity bin, and extending the isochrones to the very low-mass (VLM) regime down to $0.1 M_{\odot}$, based on the models of Cassisi et al. (2000). We note that the temperatures for these stars are cooler than those in Padova00 (Vazdekis et al. 2012). A complete description of the BaSTI database can be found in Pietrinferni et al. (2004, 2006, 2009, 2013) and Cordier et al. (2007). We adopted the non-canonical BaSTI models with the mass loss efficiency of the Reimers law (Reimers 1977) set to $\eta = 0.4$. The initial He mass fraction ranges from 0.245 to 0.303, for the more metal-poor to the more metal-rich composition, respectively, with $\Delta Y/\Delta Z \approx 1.4$.

The main sequence (MS) loci are in good agreement between these two set of models. The turn-off (TO) stars are also in good agreement for old stellar populations, but their luminosities differ for young and intermediate age regimes. The BaSTI isochrones show systematically cooler red giant branch (RGB) stars at low metallicities, but a hotter RGB in the high metallicity regime. Due to differences in the adopted mass-loss efficiency along the RGB, the core He-burning stage is hotter in the BaSTI models. Conversely, this situation reverses for young ages with the Padova00 models showing more extended blue loops, due to the treatment of convection of the He-burning core in intermediate-mass stars. Both sets of models include the TP-AGB regime using simple synthetic prescriptions. We note that the synthetic-AGB treatment in the BaSTI isochrones account for AGB nucleosynthesis, i.e. the effects of the third dredge-up and hot-bottom burning, including the related evolutionary effects. In particular the effect of the change in the envelope C/O ratio induced by the third dredge-up was mimicked by adopting a radiative opacity at a constant heavy elements distribution, but allowing the global metallicity to change. It has been shown that the population synthesis models based on the BaSTI AGB-extended models provide integrated colours that match the observations of super star clusters with intermediate ages (Noel et al. 2013). We refer the interested reader to Cassisi et al. (2004), Pietrinferni et al. (2004) and Vazdekis et al. (2015) for a more detailed comparison of these two sets of isochrones.

The theoretical parameters of these isochrones are transformed to obtain stellar fluxes using empirical relations between colours and stellar parameters (T_{eff} , $\log g$, $[\text{Fe}/\text{H}]$). We use the metallicity-dependent empirical relations of Alonso, Arribas & Martínez-Roger (1996) and Alonso, Arribas & Martínez-Roger (1999) for dwarfs and giants, respectively to obtain stellar fluxes. These relations link the colours to the stellar parameters (T_{eff} , $\log g$, $[\text{Fe}/\text{H}]$) based on two extensive photometric stellar libraries of dwarfs and giants (around ~ 500 stars each library). We use the empirical compilation of Lejeune, Cuisinier & Buser (1997, 1998) (and references therein) for the coolest dwarfs ($T_{\text{eff}} \lesssim 4000$ K) and giants ($T_{\text{eff}} \lesssim 3500$ K) for solar metallicity, and also for stars with temperatures above ~ 8000 K. A semi-empirical approach for the low temperature stars at other metallicities is used by combining these rela-

tions and the model atmosphere predictions of Bessell et al. (1989, 1991) and the library of Fluks et al. (1994). Finally, we also use the metal-dependent bolometric corrections of Alonso, Arribas & Martínez-Roger (1995) and Alonso et al. (1999) for dwarfs and giants, respectively. We adopt $BC_{\odot} = -0.12$. Assuming $V_{\odot} = 26.75$ (Hayes 1985) we obtain for the sun the absolute magnitude $M_{V_{\odot}} = 4.82$ and $M_{\text{bol}_{\odot}}$ is given by $M_{V_{\odot}} + BC_{V_{\odot}} = 4.70$.

2.2 Stellar spectral libraries

To compute both the SBF and SSP spectra at moderately high resolution we employ a variety of extensive empirical stellar spectral libraries depending on the wavelength range. We refer the interested reader to Vazdekis et al. (2016) for a complete description of the model construction which we briefly summarize here. We employ the MILES library (Sánchez-Blázquez et al. 2006), with the atmospheric parameters of Cenarro et al. (2007), to build up our reference models in the optical range (Vazdekis et al. 2010). The NGSL library (Gregg et al. 2006), as fully characterized in Koleva & Vazdekis (2012), feed our models in the UV range. To extend our model predictions out to $5 \mu\text{m}$ we employ the Indo-US (Valdes et al. 2004), CaT (Cenarro et al. 2001a,b) and IRTF (Cushing et al. 2005; Raynier et al. 2009) stellar libraries, as described in (Vazdekis et al. 2012), Röck et al. (2015) and Röck et al. (2016). In the context of the SBFs it is particularly important to emphasize here that the IRTF library that we use for the predictions in the near-IR covers all the relevant phases of the more evolved stars such as the AGBs, including five Carbon Stars. However this library has a rather limited metallicity coverage spanning around solar metallicity. These two aspects, together with the reduced number of stars (~ 180) that compose the IRTF library, limit the quality of our model predictions in the near-IR spectral range, particularly for intermediate-age regimes and for metallicities outside the range ($-0.4, +0.2$) (see for details Röck et al. 2015; Vazdekis et al. 2015).

All the atmospheric parameters of these libraries have been homogenized, and placed on the system of Cenarro et al. (2007). However not all the stars were used for computing the models as we checked every single star spectrum and discarded those with peculiarities, e.g., signs of spectroscopic binaries. In the less severe cases we just decreased their contributing weight within the interpolating algorithm. We refer the reader to the above papers for the full details.

2.3 IMF shapes

For the IMF, $\Phi(m) = dN/dm$, we adopt the multi-part power-law IMFs of Kroupa (2001), i.e. universal and revised, the two power-law IMFs described in Vazdekis et al. (1996), often regarded as “unimodal” and “bimodal”, both characterised by the logarithmic slope ($dN/d(\log m)$), Γ and Γ_b , respectively, and the Chabrier (2001) single-stars IMF. Note that the Salpeter (1955) IMF is obtained by adopting the unimodal IMF with $\Gamma = 1.35$, and the Kroupa Universal IMF is very similar (although not identical) to a bimodal IMF with slope $\Gamma_b = 1.3$.

3 MODEL SBF SPECTRA COMPUTATION

A single-age, single-metallicity stellar population, SSP, can be understood as a probability distribution that is mainly characterized by a mean $L_{\lambda}^{\text{SSPmean}}$ and a variance $L_{\lambda}^{\text{SSPvar}}$ (see [Cerviño & Luridiana 2006](#), for details). However it is worth noting that when computing SSPs it is a common practice to provide only the mean spectrum of the population. Therefore in its traditional use the SSP is regarded as the mean value of the distribution and it can be identified as

$$L_{\lambda}^{\text{SSP}} \equiv L_{\lambda}^{\text{SSPmean}} \quad (1)$$

Here we follow the "base" modelling approach described in [Vazdekis et al. \(2015\)](#) to compute the SBF spectrum corresponding to the SSP. To obtain the mean SSP spectrum, $L_{\lambda}^{\text{SSPmean}}$, we basically integrate the stellar spectra along the isochrone of the various empirical libraries described in Section 2.2. The resulting E-MILES $L_{\lambda}^{\text{SSPmean}}$ model is then used as the reference spectrum over which we calculate the corresponding variance spectrum. We compute $L_{\lambda}^{\text{SSPmean}}$ as follows

$$\begin{aligned} L_{\lambda}^{\text{SSPmean}} &= \int_{m_1}^{m_t} S_{\lambda_{\text{ref}}}(m, t, [\text{Fe}/\text{H}]) F_{\lambda_{\text{ref}}}(m, t, [\text{Fe}/\text{H}]) N_{\Phi}(m, t) dm \\ &= \int_{m_1}^{m_t} L_{\lambda}(m, t, [\text{Fe}/\text{H}]) N_{\Phi}(m, t) dm \end{aligned} \quad (2)$$

where $S_{\lambda_{\text{ref}}}(m, t, [\text{Fe}/\text{H}])$ is the empirical stellar spectrum, normalised in a reference wavelength interval λ_{ref} , corresponding to a star of mass m and measured metallicity $[\text{Fe}/\text{H}]$, which is alive at the age t of the SSP. $F_{\lambda_{\text{ref}}}(m, t, [\text{Fe}/\text{H}])$ is the flux of the star in the reference wavelength interval. Hence $L_{\lambda}(m, t, [\text{Fe}/\text{H}]) = S_{\lambda_{\text{ref}}}(m, t, [\text{Fe}/\text{H}]) F_{\lambda_{\text{ref}}}(m, t, [\text{Fe}/\text{H}])$ is the luminosity assigned to each star for their given evolutionary parameters m , t and $[\text{Fe}/\text{H}]$. Finally, $N_{\Phi}(m, t)$ is the probability that the system contains a star with a given mass. Note that this value is given by the IMF for the SSP with a given age, but it could also refer to the case of complex Star Formation Histories (SFHs). The units of the mean SSP spectra, $L_{\lambda}^{\text{SSPmean}}$, are $\text{erg s}^{-1} \text{\AA}^{-1}$. We apply a mass normalization by the mean mass of a star as given by the IMF, $\langle m \rangle$, to provide units of $\text{erg s}^{-1} \text{\AA}^{-1} M_{\odot}^{-1}$. Note that such a *a posteriori* normalization allows us to scale the obtained luminosity to that of a stellar system with any given mass.

To calculate the SBF spectrum, $L_{\lambda}^{\text{SSPsf}}(t, [\text{M}/\text{H}], \Phi)$, of the SSP with age t , total metallicity $[\text{M}/\text{H}]$, and IMF Φ , we need both the mean $L_{\lambda}^{\text{SSPmean}}$ and the variance $L_{\lambda}^{\text{SSPvar}}$ spectra of the SSP. The variance spectrum, also regarded as σ^2 , i.e. the square of the standard deviation³ σ around the mean that is taken as reference spectrum

$$L_{\lambda}^{\text{SSPvar}} = \int_{m_1}^{m_t} L_{\lambda}^2(m, t, [\text{Fe}/\text{H}]) N_{\Phi}(m, t) dm - (L_{\lambda}^{\text{SSPmean}})^2 \quad (3)$$

The variance units are $\text{erg}^2 \text{s}^{-2} \text{\AA}^{-2}$, i.e. the same ones as $(L_{\lambda}^{\text{SSPmean}})^2$ before the mass normalization (otherwise the right

hand side terms of Eq. 3 would have different units). Once again, if divided by the mean mass of a star as given by the IMF we obtain $\text{erg}^2 \text{s}^{-2} \text{\AA}^{-2} M_{\odot}^{-1}$ (note that the correct mass normalization of the variance is M_{\odot}^{-1} and not M_{\odot}^{-2} ; we refer to [Cerviño & Luridiana 2006](#); [Cerviño 2013](#), for an in-depth discussion). The subtracting term $(L_{\lambda}^{\text{SSPmean}})^2$ in Eq. 3 is the variance of the SSP as shown in [Cerviño & Luridiana \(2006\)](#) and [Cerviño et al. \(2008\)](#). Note, however, that this term is usually omitted in SBF modeling works under the assumption of Poissonian statistics in the number of stars along different element resolutions. However, this term only accounts for the $\sim 0.1\%$ of the final fluctuation (see [Cerviño et al. 2008](#), for details and further discussion). On the other hand, we note that this term is included in the observational approach as shown in Section 1 and Appendix B. Note that the subtracting term must be applied before any mass normalization of $L_{\lambda}^{\text{SSPmean}}$.

Finally, the SBF spectrum is computed as the ratio between the variance and the mean SSP spectra

$$L_{\lambda}^{\text{SSPsf}}(t, [\text{M}/\text{H}], \Phi) = \frac{L_{\lambda}^{\text{SSPvar}}(t, [\text{M}/\text{H}], \Phi)}{L_{\lambda}^{\text{SSPmean}}(t, [\text{M}/\text{H}], \Phi)} \quad (4)$$

Irrespective of whether $L_{\lambda}^{\text{SSPsf}}(t, [\text{M}/\text{H}], \Phi)$ is computed with or without applying any mass normalization, the fluctuation spectra units are $\text{erg s}^{-1} \text{\AA}^{-1}$. It is advantageous to provide separately the variance spectrum associated to the mean SSP spectrum, instead of providing simply the SBF spectrum. Among other applications, it allows one to calculate the variance of a complex SFH by a direct integration of the variance associated with each individual SSP in the SFH, in a similar way as is performed for the mean flux (see Section 4.1). We stress that the variance properties are not shared by the SBF as we show below.

In the integration of both the mean and variance, each stellar spectrum is also characterized by its T_{eff} and $\log g$ parameters, and we scale each spectrum according to the flux in the broad-band V filter. This flux is derived following the same empirical photometric relations applied to the theoretical isochrones. Before scaling we first normalise each stellar spectrum by convolving it with the filter response of [Buser & Kurucz \(1978\)](#). We follow the method described in [Falcón-Barroso et al. \(2011\)](#) that is based on the calibration of [Fukugita, Shimasaku & Ichikawa \(1995\)](#) to assign the absolute flux to the V -band. The zero-point is established by the Vega spectrum of [Hayes \(1985\)](#) with a flux of $3.44 \times 10^{-9} \text{ erg cm}^{-2} \text{s}^{-1} \text{\AA}^{-1}$ at 5556\AA , and the V magnitude is set to 0.03 mag, which is consistent with [Alonso et al. \(1995\)](#). Finally, for the spectral range beyond $\sim 9000 \text{\AA}$, we use as a reference the K band as described in [Röck et al. \(2015\)](#).

We apply a local interpolation scheme as described in [Vazdekis et al. \(2003\)](#) (see their Appendix B), and updated in [Vazdekis et al. \(2015\)](#), to calculate a stellar spectrum for a given set of atmospheric parameters. This algorithm is particularly suitable to overcome the gaps and asymmetries present in the parametric distribution of any empirical library. Note that a requested stellar spectrum is calculated according to the stellar parameters (T_{eff} , $\log g$, $[\text{Fe}/\text{H}]$), irrespective of the evolutionary stage. It has been shown that such prescription might not be sufficient to model the behaviour of the CO feature as a function of temperature in the K band, particularly for cool AGB stars

³ We recall that in this context, the standard deviation is just a measure of the variance, but it does not assume any hypothesis about the underlying distribution. As it is, this standard deviation cannot be used to establish confidence intervals unless the underlying distribution is proven to be Gaussian.

(Mármol-Queralto et al. 2008). This limitation might have a non-negligible effect on the SBF spectra of intermediate-ages, particularly at red wavelengths.

We remark here that our models employ both solar-scaled isochrones and empirical stellar libraries. Therefore these models, for which we assume that $[M/H] = [Fe/H]$, can be considered “base” models following the description provided in Vazdekis et al. (2015). Because the library spectra follow the Milky-Way abundance pattern with metallicity, the computed models are nearly consistent and solar-scaled around solar metallicity. At subsolar metallicities they lack consistency as these models combine solar-scaled isochrones with α -enhanced star spectra. We refer the interested reader to Vazdekis et al. (2015) for a version of the SSP spectra that is self-consistent in the optical range. Hereafter we use $[Fe/H]$ for the metallicity of the stars of the empirical libraries feeding the models as these are measured iron abundance values. However as the models are computed on the basis of the total metallicity we use $[M/H]$ for the resulting predictions, which are identical only in the case of the solar-scaled assumption implicit in the base modelling approach.

The model spectra in the various spectral ranges, which are computed in a fully consistent manner with the same population synthesis code, are joined as described in detail in Vazdekis et al. (2016). To summarize, we identify spectral regions where no major features are found for the range of ages and metallicities covered by our models. The overlapping windows have been chosen to be sufficiently wide to reach enough statistics for the continuum counts and, at the same time, to avoid the presence of strong spectral features. Finally, we re-scale, using the selected windows, the spectra blueward and redward of the MILES range to match the continuum of the different models based on the MILES library, which is taken as reference. Note that this approach is possible due to the good flux calibration quality of the stellar spectra of the various libraries. We apply this joining strategy to obtain both the E-MILES SSP spectra and the corresponding variance spectra. Finally, we divide the two as previously mentioned in Eq. 4 to obtain the E-MILES SBF spectra.

Figure 1 (middle panel) shows the SBF spectrum of a stellar population with solar metallicity and 10 Gyr computed with the BaSTI and Padova00 evolutionary models (see Sect. 2.1). For comparison, the figure shows in the upper panel the corresponding SSP spectrum. Note that, given the construction of the SBF spectrum, some features of the SSP get amplified. For example, we see that the drop in flux toward the UV spectral range is far more severe in the SBF spectrum than in the SSP spectrum. However we also recall that the employed isochrones do not include the white dwarfs sequence and, therefore, the UV contribution is dominated by hotter stars in the MS and also in the Horizontal Branch (HB). The latter is only relevant for metal-poor stellar populations, while for the plotted SBF spectrum (old metal-rich) the main contribution in the UV comes from the upper-MS. However these evolutionary phases are statistically far more populated, covering a relatively small range of luminosities. Another important difference is that whereas the SSP spectrum peaks around the V band, the SBF spectrum peaks around the J or H bands. This arises because in the SBF spectra the contributions from red luminous evolved stars are emphasized with respect to other phases.

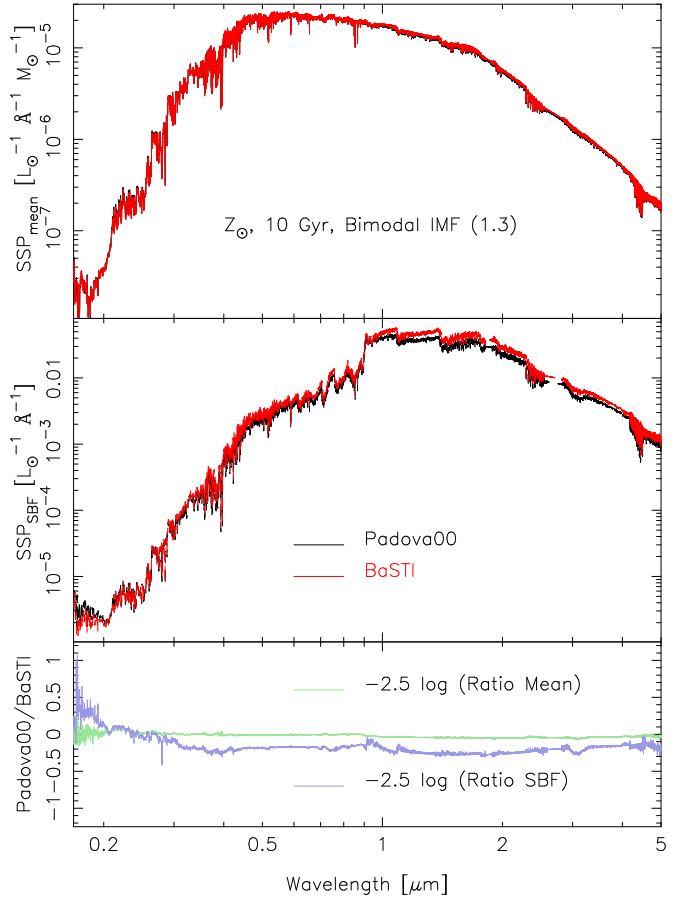


Figure 1. E-MILES SSP (top panel) and SBF (middle panel) spectra of a stellar population of 10 Gyr, solar metallicity and standard IMF (bimodal shape with logarithmic slope 1.3). We show the spectra computed with BaSTI (black) and Padova00 (red) isochrones. In the bottom panel we show the ratio of the models computed with different isochrones for the two, the mean SSP spectra (green) and the SBF spectra (blue).

It is precisely for this reason that the SBF spectrum also shows significant molecular bands in comparison to the SSP spectrum. This is clearly illustrated in the spectral region covered by the prominent CaII triplet feature in the SSP spectrum at around $\sim 8500 \text{ \AA}$, which is almost completely buried by the surrounding molecular bands in the SBF spectrum. Finally, as expected, we see that in this age and metallicity regime the choice of evolutionary models, Padova00 and BaSTI, has a significantly larger impact on the synthesized SBF spectra in comparison to the SSP spectra (see also Sect. 3.3.2).

3.1 Optical SBF model spectra with varying $[Mg/Fe]$ -abundance

We also compute a set of models with varying $[Mg/Fe]$ abundance ratio for the MILES spectral range to assess the effect of this parameter on the resulting optical SBF spectra. For this purpose we use the $[Mg/Fe]$ -enhanced and solar-scaled version of our models that are described in Vazdekis et al. (2015). Briefly, the models employ the theoretical stellar

spectral library of Coelho et al. (2005), with its extension to cool stars of Coelho et al. (2007), to obtain SSP-based differential spectral corrections. For this purpose the models employ the BaSTI solar-scaled and α -enhanced isochrones of Pietrinferni et al. (2004, 2006), which are calculated with similar $[\alpha/\text{Fe}]$ abundance ratios to the stellar atmospheres. The isochrones are converted to the observational plane using the photometric stellar libraries described in Section 2.1. We take into account the $[\text{Mg}/\text{Fe}]$ determinations for the MILES stars of Milone et al. (2011) to compute reference models based exclusively on the MILES database. Note that we use these $[\text{Mg}/\text{Fe}]$ values as a proxy for the $[\alpha/\text{Fe}]$ values of the MILES stars. For this reason we refer to the resulting models as $[\text{Mg}/\text{Fe}]$ -enhanced instead of $[\alpha/\text{Fe}]$ -enhanced. Finally we correct these reference SSP models with the corresponding SSP-based theoretical spectral responses to obtain the enhanced SSP models.

It is worth recalling here that these models are self-consistent in the sense that both ingredients, the theoretical stellar spectra and the isochrones are computed with the same overall α -enhancement. These models are computed for two $[\text{Mg}/\text{Fe}]$ -enhancement values: 0.0 and 0.4. The $[\text{Mg}/\text{Fe}]$ -enhanced models have an iron content that differs by $\Delta[\text{Fe}/\text{H}] = -0.3$ with respect to the total metallicity $[\text{M}/\text{H}]$ (see Vazdekis et al. 2015). For example, the $[\text{Mg}/\text{Fe}]$ -enhanced SBF model spectra with $[\text{M}/\text{H}] = +0.06$ have $[\text{Fe}/\text{H}] = -0.24$, whereas the solar-scaled spectra verify $[\text{M}/\text{H}] \equiv [\text{Fe}/\text{H}]$.

3.2 Models coverage

The newly computed model spectra cover the wavelength range $\lambda\lambda$ 1680.2 Å–49999.4 Å at moderately high spectral resolution. As the models employ varying stellar spectral libraries, we have decided to keep their nominal resolutions in most of the spectral ranges. This includes a change from a constant FWHM resolution to a constant σ resolution at 8950 Å. Note for example in Fig. 1 the change in resolution from 5 to 2.51 Å (FWHM) blueward 3541.4 Å, or that from FWHM = 2.5 Å to $\sigma = 60 \text{ km s}^{-1}$ redward 8950 Å (FWHM = 4.2 Å at that wavelength). The spectra have been rebinned to a linear dispersion of 0.9 Å/pix along the whole spectral range.

The E-MILES SBF spectra span a rather wide age interval, including ages below 1 Gyr. However the SBF predictions for ages below 3 Gyr are far more sensitive to the modelling details as in, e.g., the mass-loss along the AGB (Raimondo et al. 2005); see also González-Lópezlira et al. (2010); González-Lópezlira (2018). Regarding the metallicity coverage the SBF spectra computed with the Padova00 models are provided for the following metallicity bins $Z = 0.0004, 0.001, 0.004, 0.008, 0.019$ and 0.03, or, alternatively, $[\text{M}/\text{H}] = -2.32, -1.71, -1.31, -0.71, -0.40, 0.0$ and 0.22, respectively. On the other hand the models based on BaSTI are provided for the following metallicity bins: $Z = 0.0001, 0.0003, 0.0006, 0.001, 0.002, 0.004, 0.008, 0.0100, 0.0198, 0.0240, 0.0300$ and 0.0400, or, alternatively, $[\text{M}/\text{H}] = -2.27, -1.79, -1.49, -1.26, -0.96, -0.66, -0.35, -0.25, 0.06, 0.15$ and 0.26, respectively. With respect to the IMF shape, apart from the Chabrier and the two Kroupa IMFs, we vary the slope of the unimodal and bimodal IMF functional

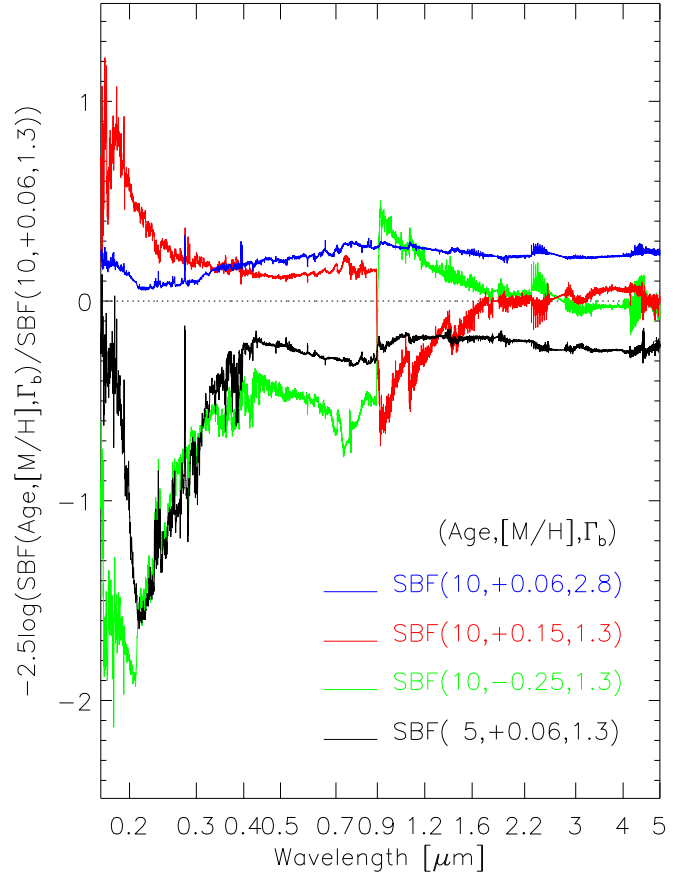


Figure 2. The sensitivity of the SBF spectra to relevant stellar population parameters is illustrated as a difference in magnitude. SBF spectra with varying metallicity ($[\text{M}/\text{H}] = 0.15$ and $[\text{M}/\text{H}] = -0.25$ vs. $[\text{M}/\text{H}] = 0.06$ in red and green, respectively) for the same age (10 Gyr) and IMF (bimodal with logarithmic slope $\Gamma_b = 1.3$). SBF spectra with varying age (5 vs. 10 Gyr), same metallicity ($[\text{M}/\text{H}] = 0.06$) and IMF slope ($\Gamma_b = 1.3$) is shown in black. Finally SBF spectra with varying IMF, bottom-heavy ($\Gamma_b = 2.8$), which is characteristic of massive ETGs, and standard ($\Gamma_b = 1.3$), with the same age (10 Gyr) and metallicity ($[\text{M}/\text{H}] = 0.06$) is shown in blue. Note that each of the varying models, whose parameters are indicated within parenthesis (age, metallicity and IMF slope) are compared allways to the same reference SBF spectrum (10, +0.06, 1.3). All the models are computed with the BaSTI isochrones.

forms. Specifically, we compute SBF spectra for top-heavy IMF slopes (0.3) to very bottom-heavy (3.5).

The quality of the computed models depend to a great extent on the input stellar libraries, which vary in their atmospheric coverage and density of stars. We refer the interested reader to Vazdekis et al. (2016) for a full characterization of the quality in the various spectral ranges covered by E-MILES models. All these models can be downloaded from the MILES website <http://miles.iac.es>.

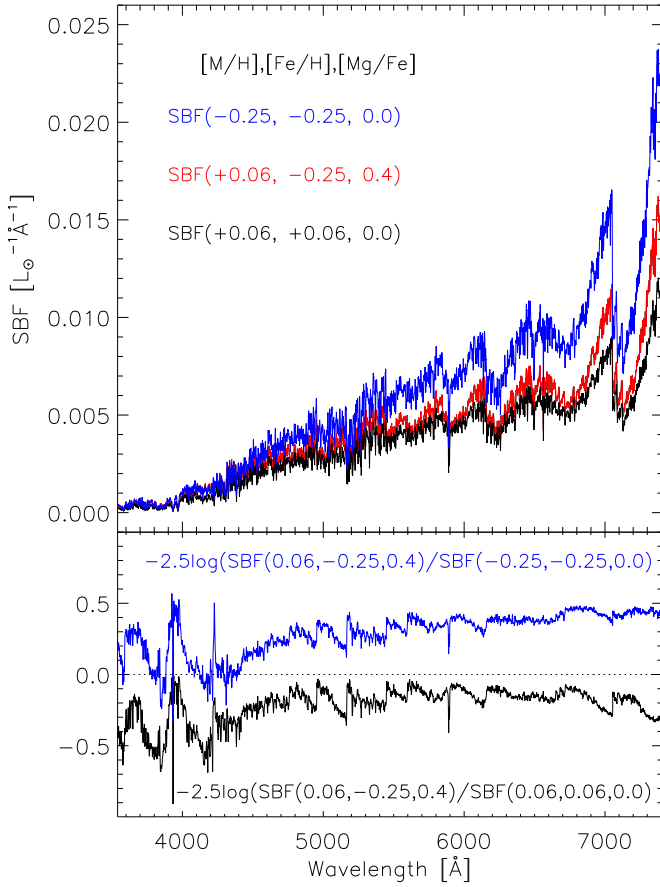


Figure 3. The upper panel shows SBF spectra with constant total metallicity ($[M/H] = 0.06$) and varying abundance ($[Mg/Fe] = 0.0$ plotted in black and $[Mg/Fe] = 0.4$ plotted in red). These two models differ in their $[Fe/H]$ content ($[Fe/H] = 0.06, -0.25$). Also plotted (in blue) is a solar-scaled model with similar iron abundance ($[Fe/H] = -0.25$) but differing total metallicity ($[M/H] = -0.25$) with respect to the α -enhanced model. All the spectra are computed with the BaSTI models and have similar age (10 Gyr) and IMF (bimodal with logarithmic slope $\Gamma_b = 1.3$). The sensitivity of these two solar-scaled SBF spectra with respect to the α -enhanced model is shown in the lower panel as a difference in magnitude.

3.3 Behaviour of the models

3.3.1 Variation with stellar population parameters

In this section we describe the behaviour of the SBF spectra with relevant stellar population parameters. Figure 2 shows the difference in magnitude obtained for SBF spectra with varying metallicity, age and IMF. We see that the SBF spectra are mostly sensitive to the metallicity and age, particularly in the UV and optical spectral ranges. This variation in the blue spectral range is not surprising since the TO (hot) stars are positioned in the blue part of the HR diagram. The sensitivity to age and metallicity is roughly similar in shape, although some differences can be seen in the bluest end. On the contrary, the SBF spectral sensitivity obtained when the metallicity is varied shows larger differences in the near-IR, mostly related to the relatively stronger molecular bands and steeper SBF spectrum shape of the more metal-rich model.

More importantly, such differences indicate potential capabilities at breaking the age metallicity degeneracy using the SBF spectra (see also Buzzoni 2005).

Figure 2 shows that the IMF remains as a second order effect on the SBF spectra. This is not surprising for such an old age regime as in the computation of an SBF spectrum the relative contribution of the brightest, more evolved, stars is emphasized. As these stars span a rather narrow initial mass range there is not enough contrast to discern the contribution of lower mass stars, whose contribution has decreased in the computation of the variance compared to their contribution in the SSP spectrum. Therefore the main effect of steepening the IMF slope is that we obtain a slightly fainter SBF spectrum.

It is worth noting that such sensitivities and the fact that elliptical galaxies show radial variations of metallicity, abundance ratios, age and IMF (e.g. Martín-Navarro et al. 2015, 2018), might have a non-negligible impact on the SBF measurements in different regions of a galaxy and resulting SBF gradients (e.g., Tonry 1991; Sodemann & Thomsen 1995, 1996; Luppino & Tonry 1993). On the other hand, these results point to a potential use of the SBF spectra to constrain relevant stellar population parameters.

Finally we also study the behaviour of the SBF spectra with varying $[\alpha/Fe]$ abundance. This is illustrated in Fig. 3 for the MILES spectral range. Overall we find that at constant total metallicity the α -enhanced SBF models are around 0.1 – 0.2 mag brighter in most of the spectral range covered by the MILES spectral range, being even brighter at the bluest and reddest ends. On the contrary, the α -enhanced model is fainter by 0.3 – 0.4 mag if the $[Fe/H]$ content is kept constant. In the two cases we find both a colour term as well as significant variations related to the molecular bands, throughout the covered spectral range. The obtained differences can be very useful at aiding SBF distance-based calibrations (see Section 6.1).

3.3.2 Variation with the input isochrones

In addition to the variation with stellar population parameters, we also test here the effects of using different evolutionary tracks on the SBF spectrum. Fig. 1 shows the SBF spectra computed with two sets of isochrones. In particular, the bottom panel shows the ratio of the mean values (SSPs) and the ratio of the SBFs obtained with the Padova00 and BaSTI models. We note that the metallicities between both set of tracks are not identical, however such a difference has a minor impact on this comparison. We find that the ratio of mean values (SSPs) shows almost negligible differences, except in the blue range ($\sim 10\%$, percentage of difference). On the contrary the SBF ratio shows significantly larger variations throughout the whole spectral range covered by the models. In fact the SBF ratio highlights differences at short and large wavelength scales, which are related to differences in the molecular bands and in the continuum. These two effects can be attributed in part to differences in the temperature of the RGB evolutionary phase and in the characteristic lifetimes of these stars. We refer the reader to Vazdekis et al. (2015) for a more elaborated discussion on the main differences between these two sets of isochrones for the mean SSPs. See also Marín-Franch & Aparicio (2006) for the effects of varying the isochrones on the SBF mag-

nitudes. The impact of varying the stellar evolutionary prescriptions on the SBF magnitudes is also discussed in [Raimondo et al. \(2005\)](#); [González-Lópezlira et al. \(2010\)](#); [González-Lópezlira \(2018\)](#).

The observed differences in the SBF spectra translate to differences in the SBF photometry, as shown in Sections 4.2 and 6.1. However the SBF spectra provide us with the advantage of studying these differences with great detail, including how spectral indices would fluctuate according to the selected isochrone set, hence providing an additional test for validating these models. It is worth recalling here that the SBF is a global property of the population, rather than being associated to any given stellar type. Therefore the SBF is more sensitive than the mean value (i.e., the SSP) to the lifetimes of the different stellar types in the ensemble as mentioned above.

4 USE OF THE SBF SPECTRA

A relevant peculiarity of the SBF spectrum is that it is not a spectrum in the standard meaning, but rather a ratio between a variance and a mean spectrum. Consequently, these two spectral components must be treated separately in any step, as explained in the following sections. We focus here on some of the possible uses that we envisage for these new models.

4.1 Star Formation Histories

We focus here on SBF models that are contributed by different stellar population components. Due to its definition, the SBF spectrum of a composite stellar population cannot be computed by directly combining the single-age single-metallicity SBF spectrum of each component. Instead the mean value and the variance of each SSP must be computed separately and combined afterwards to obtain the resulting SBF spectrum, as their ratio.

Prior to the computation of the SBF spectrum of a composite population we first need to *i*) combine the mean (SSP) spectra and *ii*) calculate the variance of the sum as the sum of the variances, since the different SSPs are not correlated. This is the case because a SSP at a given age is independent from any other SSP with a different age. We therefore proceed to calculate the variance as follows

$$L_{\lambda}^{\text{SFHvar}}(t) = \int_0^{\infty} \psi(t') L_{\lambda}^{\text{SSPvar}}(t' - t) dt' = \sum a_{\text{SFH}}(t') \sigma^2(t' - t) \quad (5)$$

where $\psi(t)$ is the SFH and $a_{\text{SFH}}(t)$ are the SFH coefficients when it is discretised as a combination of SSPs. We note that neither $\psi(t)$ nor $a_{\text{SFH}}(t)$ contain a squared term. In other words, this is a consequence of the scaling relations of the variance of the stellar population as a function of the stars and mass in the system (c.f. [Cerviño & Luridiana 2006](#), and [Cerviño in preparation](#))⁴. In summary, unlike the SBF spec-

⁴ In a back of the envelope argument, the use of $\psi(t)^2$ or $a_{\text{SFH}}(t)^2$ coefficients imply that the resulting SBF spectrum would depend on the SFH normalization; whereas using $\psi(t)$ or $a_{\text{SFH}}(t)$ the SFH normalization in the variance cancels out with the corresponding SFH normalization of the mean (when is computed the SBF).

tra, the variance spectra can be treated in the same way as the mean spectra for the computation of composite stellar populations. Finally, it is worth noting that such an approach is valid as far as the stellar birth-rate function can be described by the SFH and IMF, and both functions can be treated separately (i.e. the IMF is independent of the SFH). Note that this is a rather common assumption (see the basic modelling approach described in [Tinsley 1980](#)). If these two functions are not independent of each other it would then become necessary to obtain the correlation among the various SSPs under a given set of stellar birth-rate conditions.

4.2 Wavelength resampling and spectroscopic SBF magnitudes

The manipulation of a single SBF spectrum for wavelength re-sampling and other operations concerning wavelengths also differs from the standard treatment of a mean spectrum. This happens when the fluxes in different wavelengths of a single SBF spectrum are combined to obtain a new SBF-related quantity. This applies to the computation of magnitudes from the SBF spectra (hereafter spectroscopic SBF magnitudes), equivalent widths or other spectroscopic indices involving a ratio, or when matching kinematic galaxy properties. In such cases, in addition to the general rule that mean and variance components have to be manipulated separately, it is also necessary to take into account the correlations between different wavelengths.

The main aspect to take into consideration is that we cannot assume that the SSP variance-flux at a given wavelength λ_i , $F_{\lambda_i}^{\text{var}}$, is independent of the SSP variance-flux at another λ_j , $F_{\lambda_j}^{\text{var}}$. In fact, the difference in F_{λ}^{var} for small $\Delta\lambda$ intervals should be strongly correlated, particularly in adjacent wavelengths, as the contribution to this flux originates from the same stellar types. Therefore, for a given integration function described by $T(\lambda)$, comprising a set of T_{λ_i} values with N elements, and using the standard linear model for variance propagation, we have⁵

$$F_{\text{band}}^{\text{var}} = \sum_{i=1}^N T_{\lambda_i}^2 \sigma_{\lambda_i}^2 + 2 \sum_{i=1}^N \sum_{j>i}^N T_{\lambda_i} T_{\lambda_j} \sigma_{\lambda_i} \sigma_{\lambda_j} \rho_{\lambda_i \lambda_j} \quad (6)$$

where $\rho_{\lambda_i \lambda_j}$ is the correlation coefficient between the two wavelengths and $\sigma_{\lambda_i} = \sqrt{F_{\lambda_i}^{\text{var}}}$.

As it is rather difficult task to obtain the full set of $\rho_{\lambda_i \lambda_j}$ for each SSP variance spectrum we have explored different assumptions, using simple hypotheses about $\rho_{\lambda_i \lambda_j}$ in Appendix A. We used for this purpose the *SED@* models ([Cerviño & Luridiana 2006](#), and [Cerviño in preparation](#)).

Another point is that each normalized SSP model provides the probability distribution of a single star, so that by multiplying by $a_{\text{SFH}}(i)$ we obtain the total number of stars present in each SSP. Basically, this translates the sum of individual stars into the sum of stars with a given age

⁵ We note that the trapezoidal rule employed for the integration introduces in the variance an extra covariance between adjacent bins (see, e.g., [Appendix in Castro-Almazán, Pérez-Jordán & Muñoz-Tuñón 2016](#)). We do not include this effect in Eq. 6.

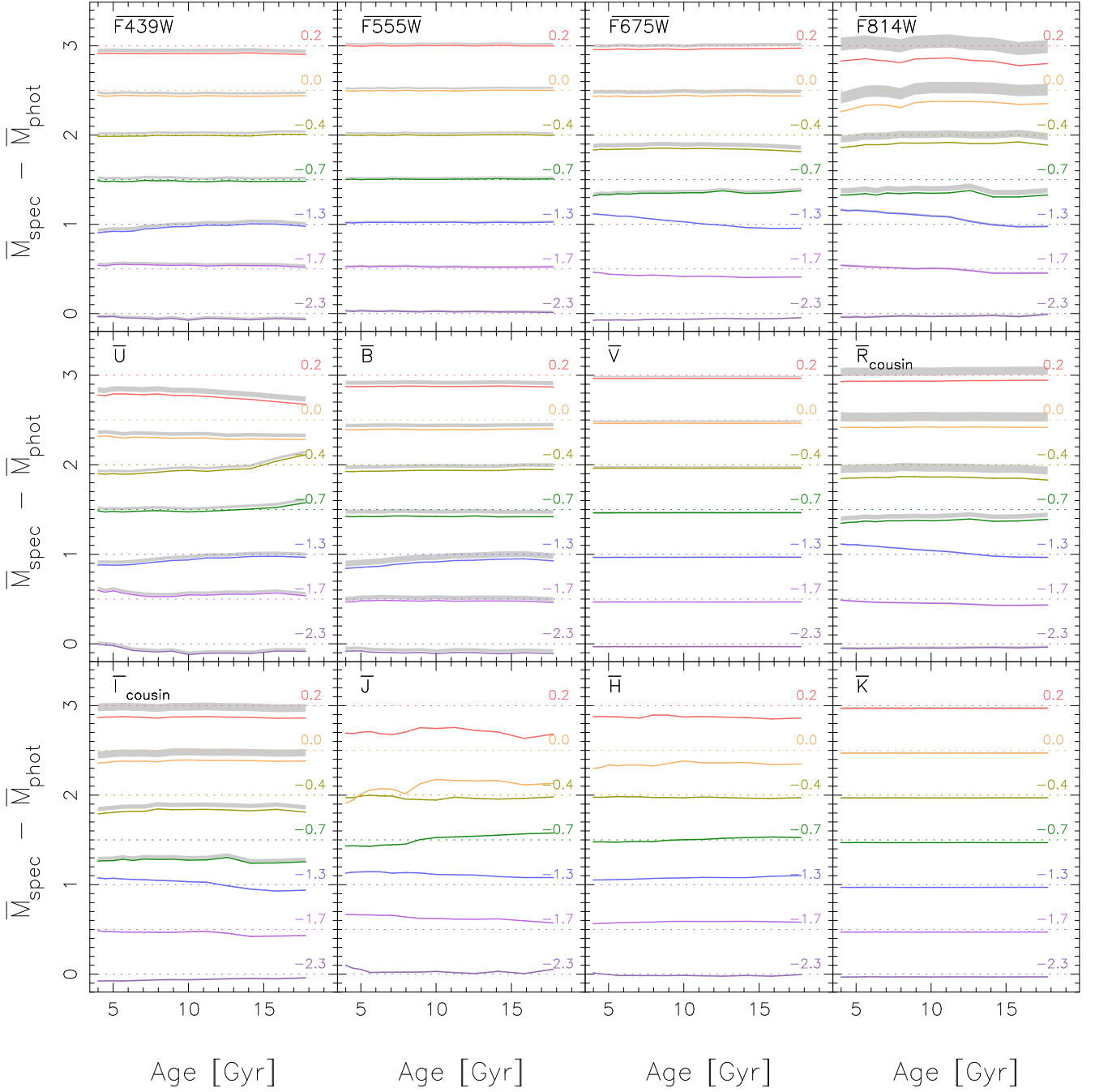


Figure 4. Internal consistency test showing the difference obtained when comparing the photometric SBF magnitude, Vega system, with the spectroscopic SBF magnitude for varying filters. The photometric values are obtained on the basis of extensive photometric stellar libraries, whereas the spectroscopic magnitudes are obtained by convolving the filter response to the variance and mean (SSP) spectra, as described in Eq. 8. For the latter the hypothesis of full-correlation between the wavelengths within the filter passband is adopted. The panels show the results for the various Johnson-Cousin broad-band filters, except for the top panels, which show the HST WFPC2 filters. The solid lines show this difference as a function of the stellar population age (in Gyr) with Padova00 isochrones and Kroupa Universal IMF. The metallicity of these models, colour coded, increase in each panel from bottom to top, shifted 0.5 magnitudes for visibility. The metallicity value is shown at the oldest age end of the perfect agreement black dotted line. The difference obtained after applying the minimum and maximum offsets due to non full correlation, as obtained in Appendix A, are shown by the dashed area. Note that for some filters such corrections are so small that it cannot be distinguished in the plot. Every tick in the vertical axis represents a fluctuation difference of 0.1 mag.

We feed these models with the same set of isochrones employed by E-MILES (Padova00 and BaSTI), but with the low resolution BaSeL3.1 semi-empirical stellar spectral libraries (Westera et al. 2002). Overall, the best results are obtained when assuming the hypothesis of a full correlation between wavelengths (i.e. $\rho_{\lambda_i \lambda_j} = 1 \forall i, j$), which transforms Eq. 6 to

$$\begin{aligned} F_{band}^{\text{var}} &= \left(\sum_{i=1}^N T_{\lambda_i} \sigma_{\lambda_i} \right)^2 \\ &= \left(\int T(\lambda) \sqrt{F_{\lambda}^{\text{var}}} d\lambda \right)^2 \end{aligned} \quad (7)$$

Finally, we can calculate the spectroscopic SBF magnitude as follows

$$\bar{m}(\text{spec}) = m_{\text{sbf}}(\text{spec}) = 2 \times m \sqrt{F_{\lambda}^{\text{var}}} - m_{F_{\lambda}^{\text{mean}}} \quad (8)$$

where \bar{m} is the standard notation of the SBF magnitude, and $m \sqrt{F_{\lambda}^{\text{var}}}$ and $m_{F_{\lambda}^{\text{mean}}}$ are the spectroscopic magnitude of the square root of the SSP variance and the mean SSP, respectively.

We note that in the case of fully correlated wavelengths we obtain the maximum possible variance. This means that the spectroscopic SBF magnitudes derived in this way are brighter than the photometric ones. Brighter fluctuations are unphysical, whereas fainter magnitudes are possible due to non full correlation within the spectral domain of the filter. Tables A1, A2 and A3 in Appendix A show the minimum and maximum offsets obtained, due to non full correlation, for the Johnson-Cousin, SDSS and HST broad band filters for different metallicities and ages. These limiting values are provided for each metallicity bin. These values are obtained by varying the age of the stellar population, for ages above 4 Gyr, and varying the input set of isochrones feeding the models. In general, the maximum differences between the spectroscopic and photometric SBF magnitudes do not exceeded 0.1 mag (in most cases they are lower than 0.04 mag), with the exception of the *I* and F814W/HST bands at solar and super-solar metallicities, see Figure A1 in appendix A for more details. We also refer the reader to Cerviño & Valls-Gabaud (2003); González et al. (2004) and Sánchez-Gil et al. (2019) for studies about the correlation between different wavelengths. By simple mathematical inspection, our approximation should work better for box-shaped filters, which only affects the integration limits, and fully correlated wavelengths within the filter domain. It is also more accurate in continuum dominated spectral regions, or when the spectrum can be approximately represented by very low order polynomials that, in practise, split the integrated area within the filter window in two similar parts.

We made use of Eq. 8 to obtain the spectroscopic SBF magnitudes. To perform an internal consistency model check, we compared these fluctuation magnitudes to those computed with the same stellar population synthesis code but following the classical approach, which integrates the fluxes in these bands Blakeslee et al. (2001), i.e. hereafter the photometric E-MILES predictions. For computing the E-MILES photometric fluctuation magnitudes we employ extensive photometric libraries, rather than spectra. These

libraries are the same ones that we use to transform the theoretical parameters of the isochrones to the observational plane, as described in detail in Section 2.1. Figure 4 shows the resulting fluctuation magnitude difference as a function of age and metallicity for representative filters from the Johnson-Cousin and HST WFPC2 Vega system, as published in Blakeslee et al. (2001) and updated here. In each panel the metallicity of the models is colour coded and shifted by 0.5 mag for visibility. The solid line is the difference between the spectroscopic fluctuation magnitudes, using Eq. 8, with respect to the corresponding photometric fluctuation magnitudes. The dotted line represents a perfect match, whereas the dashed area corresponds to the spectroscopic values after applying the minimum and maximum offsets as obtained in Appendix A, due to non full correlation between the wavelengths within the band. Such a comparison also helps in assessing the relative impact of the varying empirical libraries that feed our models for both, the photometric and the spectroscopic predictions. Besides the full correlation approximation adopted here for obtaining the spectroscopic SBF magnitudes, i.e. Eq. 8, we do not expect a perfect match. This is because the photometric and spectroscopic libraries differ in their stellar parameters coverage and other aspects such as, e.g., flux-calibration issues affecting the stellar spectra. Such aspects are likely responsible for the additional residuals that contribute to the mismatch seen in some filters. These additional offsets are larger than the ones due to non full correlation effects for the *F814W* and *R* filters, similar for the *F439W*, *F675W*, *U*, *B* and *I* filters, and negligible for the remaining ones. Note, however, that these offsets are calculated with the aid of the *SED@* models, which make use of a semi-theoretical library. Indeed, the coverage of this semi-theoretical library for cool stars is scarce in comparison to that in E-MILES. Such issues might introduce further residual fluctuation differences, which prevent us from separating more cleanly these two major sources of uncertainties. Moreover, non full covariance effects seem to be underestimated in several filters, and particularly in the *J* and *H* bands. For comparison, we note here that our photometric and spectroscopic magnitudes for the mean SSPs lead to differences that are typically within 0.02 mag (Ricciardelli et al. 2012).

Overall, the fluctuation magnitudes agree within 0.1 mag, and are smaller in most cases, but can also be as large as 0.2 mag for some filters. The spectroscopic SBF magnitudes obtained for the HST filter system show in general the best match to the photometric values. This is not surprising given the fact that these filters have a significantly more boxy-shaped transmission. The very best agreement is reached for the *V* and *K* bands for all metallicities and ages. This is not surprising given the procedure adopted to scale the individual stellar spectra during the computation of the SSP, as described in Section 3. The largest differences are found for the *J* band filter, particularly in the high metallicity regime. These fluctuation magnitude differences can be attributed in part to the huge molecular bands that are present in the *J* band of the empirical stars that feed E-MILES. Such features are not reproduced by the low resolution theoretical atmosphere models that feed the *SED@* models, leading to inaccurate offsets. We also find significant differences in the *U* and *H* filters, primarily for the most metal-rich stellar populations. The differences ob-

tained for the H band can be attributed to the same reasons affecting the J band. However, the differences affecting the metal-rich spectroscopic SBF magnitudes obtained for the U band not only originate in the strong and wide spectral features present in this band but, also, in the very steep spectrum shape that characterise the SBF spectra of old stellar populations. We discourage potential users of these SBF spectra to obtain spectroscopic magnitudes in the UV spectral region. Despite these limitations we stress here that the SBF spectra provide the flexibility that is required to convert SBF magnitudes obtained with varying photometric systems. This is particularly useful for homogenizing data coming from different sources. In fact, by applying Eq. 8 for a given filter definition to two different observational setups one can use the obtained spectroscopic magnitude difference to bring one photometric measurement to the other. Of course, this differential correction is more accurate when using the SBF spectra that correspond to the best matching mean values.

5 COMPARISON TO OTHER SBF SPECTRAL MODELS

We have compared our model spectra to the recently published SBF model spectra of Mitzkus et al. (2018). A unique and common feature of this comparison is that these authors also employ the MILES stellar database. For the other major ingredient of their population synthesis code, these authors make use of the PARSEC isochrones Bressan et al. (2012). These isochrones are a revised version of the former Padova models, with updated input physics and using the solar composition from Grevesse & Sauval (1998) and elemental abundances from Caffau et al. (2011). For the TP-AGB stars these models make use of the COLIBRI code (Marigo et al. 2017). Finally, it is worth noting that although these authors also compute SBF spectra based on a theoretical stellar library, namely that of Coelho (2014), we use here their version based on MILES to minimize the differences with our models. Their models are computed with the Chabrier (2003) IMF.

Figure 5 shows a representative SBF spectrum from these authors with solar metallicity and 10 Gyr, compared to an equivalent model computed with our code with the Padova00 isochrones. As the Mitzkus et al. (2018) spectra are not calibrated in flux, but the relative spectral shape, we scaled their SBF spectrum by an arbitrary factor to match our models. Overall we find a good agreement, although there are significant residuals at intermediate wavelength scales redward of ~ 6000 Å. These residuals are associated with the molecular bands that are present in evolved cool stars. According to Fig. 12 in Bressan et al. (2012) the brightest and coolest RGB stars in the PARSEC models are cooler than in the Padova00 that are employed in our models, although the slope of this evolutionary phase is steeper in Padova00, which makes the base of the RGB slightly cooler. These differences might suggest that the SBF spectrum by Mitzkus et al. (2018) presents deeper absorption molecular bands compared to ours, as the SBF goes as the inverse of the mean SSP spectrum. There are also other differences between the two stellar population synthesis codes, such as, e.g., the algorithm employed to assign stars from the MILES

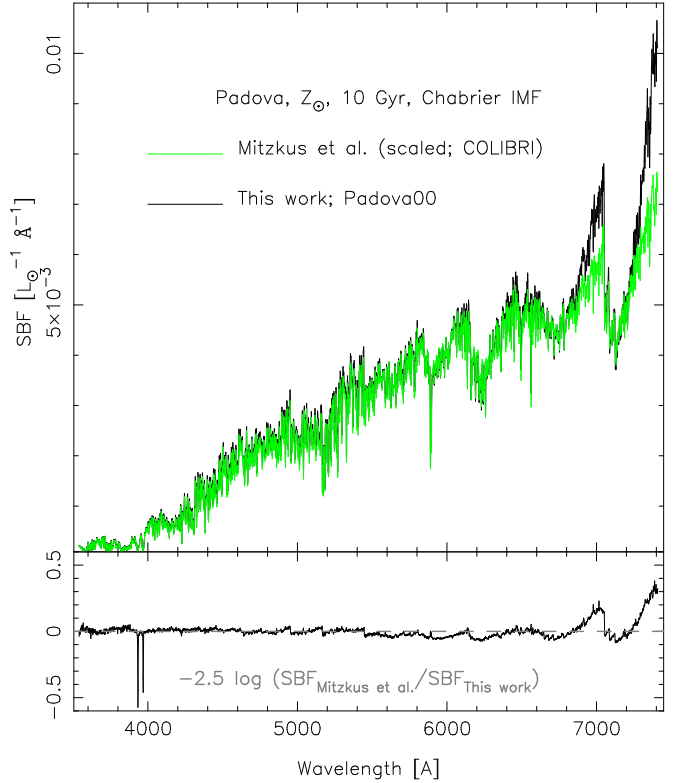


Figure 5. Comparison of our model SBF spectrum (black) with solar metallicity, 10 Gyr and Chabrier IMF, with the SBF spectrum of Mitzkus et al. (2018) (green) with similar stellar population parameters. In the bottom panel we show the residuals.

database when integrating along the isochrone. The fact that we do not see any significant colour term in the obtained residuals, but differences in the molecular bands in the red spectral range, strongly suggest that differences in the SBF spectra mostly originate in the modelling approaches related to the coolest stars near the tip of the RGB.

We also compared our SBF spectra with those of Buzzoni (1989)⁶ and the SED@ models presented in González Delgado et al. (2005)⁷ ⁸. Both set of models provide the SSP variance, although encoded as the effective number of stars N_λ . The relation between N_λ , SBF and mean SSP spectra is given by (c.f. Buzzoni 1993):

$$L_\lambda^{\text{SSPmean}} = L_\lambda^{\text{SSPvar}} \times N_\lambda \quad (9)$$

All these models are computed with the Salpeter IMF (in our case the unimodal IMF option with logarithmic slope 1.35) and are calibrated in flux, so that we can directly compare the absolute values. However, the stellar spectral libraries (theoretical in the case of these authors) and the isochrones differ between the models. The Buzzoni (1989) models include the evolution of Post-AGB stars, three different morphologies for the Horizontal-Branch and two different mass-

⁶ <http://www.bo.astro.it/~eps/models.html>

⁷ <https://www.iaa.csic.es/~rosa/research/synthesis/HRES/ESPS-HRES.html>

⁸ <http://cab.inta-csic.es/users/mcs/SED/>

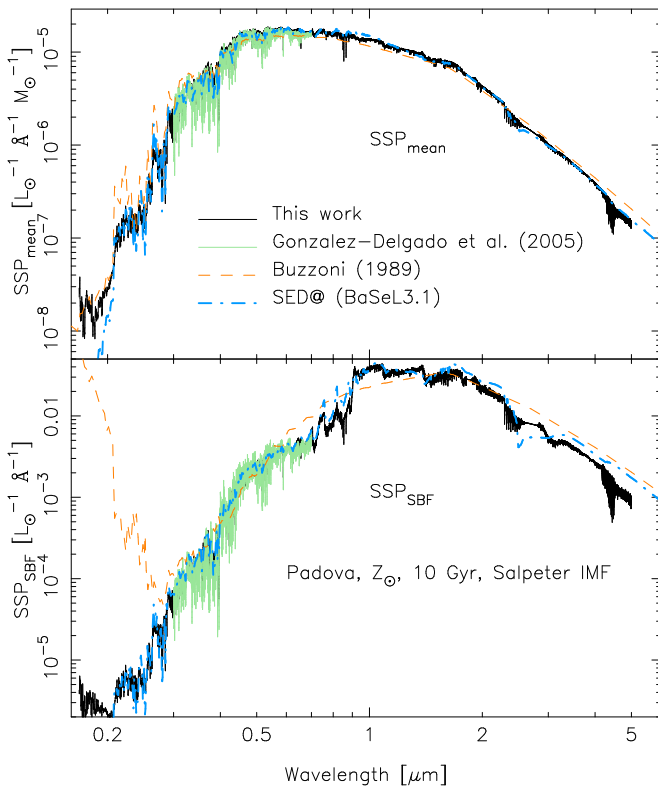


Figure 6. Comparison of our models (solid black) with solar metallicity, 10 Gyr and Salpeter IMF, with the models of [Buzzoni \(1989\)](#) (dashed orange) and [González Delgado et al. \(2005\)](#) (solid green) with similar stellar population parameters. We also include in this comparison the low-resolution *SED@* models (dot-dashed light blue) employed in Section 4.2.

loss parameters η . For the comparison with our models we selected the models with red HB morphology and $\eta = 0.3$. The *SED@* models presented in [González Delgado et al. \(2005\)](#) make use of the theoretical stellar spectral library of [Martins et al. \(2005\)](#) and the Padova00 isochrones. Figure 6 shows the SBF spectra from these authors, together with the E-MILES models. All these models were computed with the Padova00 isochrones with Salpeter IMF, 10 Gyr and solar metallicity. In addition, we also plot the low-resolution *SED@* model employed here, which was used to estimate the effects of the full correlated spectrum approach described in Section 4.2. In general, the models agree reasonably well among each other, given the varying model ingredients (we refer to [Mitzkus et al. 2018](#), for a more detailed study about the variations on stellar libraries).

6 APPLICATIONS

We show here some applications of the newly computed SBF spectra. Specifically we focus on the use of SBF magnitudes derived from these spectra.

6.1 Comparison with empirical SBF distance calibrations

The determination of galaxy distances has been a central problem in Astronomy. One of the most accurate methods to obtain distances is using SBFs as the observed flux of the fluctuations depends on the distance of the object, with more distant galaxies appearing smoother. The SBF method has given distances to Virgo and Fornax with a precision of 2% (see [Blakeslee 2012](#), for a review).

To measure distances, observational studies have aimed at accurately estimating the absolute SBF magnitude, \bar{M} , using empirical calibrations. However, as \bar{M} is an intrinsic property of the stellar populations of a galaxy, it is possible to derive these calibrations from stellar population models. Figure 7 shows the absolute SBF magnitudes in the F814W/ACS/HST band, \bar{M}_{814} , derived from SBF spectra as a function of $g_{475} - I_{814}$ colour. \bar{M}_{814} is obtained following the methodology described in Sec. 4.2 using the response of the F814W/ACS/HST filter. The mean spectra corresponding to these SSPs were used to obtain the spectroscopic g_{475} and I_{814} magnitudes by direct convolutions with the F475W and F814W/ACS/HST filters, respectively. The models used here and shown in Fig. 7 adopt a bimodal IMF with a slope of 1.3 for the Padova00 (left panel) and BaSTI (right panel) isochrones. Each point is colour-coded according to its metallicity from purple, $[M/H] = -2.3$, to red, $[M/H] = 0.26$. Symbol size increases with age, and we plot ages from 4 to 13 Gyr. The solid black line is the calibration given in Eq. 2 in [Blakeslee et al. \(2010\)](#), derived from early-type galaxies in the Fornax cluster. Contrary to what is expected for massive ETGs, this calibration lies at metallicities slightly lower than solar metallicity.

Apparently these lower inferred metallicities might be an indication of metallicity gradients, as observed in elliptical galaxies (e.g., [Montes et al. 2014](#); [Martín-Navarro et al. 2018](#)), which lowers the total integrated metallicity observed in these galaxies. [Blakeslee et al. \(2010\)](#) measured their SBF magnitudes at radii between $6''.4$ to $32''$ where steep metallicity gradients are observed in early-type galaxies (e.g., [Sánchez-Blázquez et al. 2007](#); [Spolaor et al. 2010](#)). In fact, [Cantiello et al. \(2005, 2007\)](#) found that the size of the internal SBF-colour slope for multiple annuli in their sample of galaxies observed with ACS/HST is related in most cases to metallicity gradients, although in some cases to age gradients. Since the presence (or absence) of a SBF gradient is connected to the properties of the dominant stellar population, it could be used as a tracer of the formation scenario of the galaxy ([Cantiello et al. 2011](#)). A more detailed discussion on the connection between these gradients and the derived SBF magnitudes can be also found in, e.g., [Tonry \(1991\)](#); [Jensen et al. \(1998\)](#); [Cantiello et al. \(2005\)](#). Such gradients should be properly taken into account when deriving SBF magnitudes in galaxies for very precise distance determinations. The SBF signal and the galaxy colour should be obtained in the same region of the galaxy.

The fact that our SBF models point toward lower metallicities can be attributed in part to the physical ingredients in stellar evolution, and stellar libraries, employed for computing the SBF spectra, from which these magnitudes are derived. This is shown in Fig. 7, where the fluctuation magnitudes predicted on the basis of the Padova00

models place the empirical distance calibration at relatively lower metallicities than those from the BaSTI models. Moreover, the fact that the most massive galaxies show [Mg/Fe]-enhancement (e.g., [Renzini 2006](#)) might have non-negligible implications. In Fig. 3 we showed that at constant total metallicity the [Mg/Fe]-enhanced models with solar metallicity are brighter than their solar-scaled counterparts by at least 0.2 mag around ~ 7000 Å. Correcting this difference will bring our solar metallicity models on the top of the distance SBF calibration. These results are along the lines of those shown by [Lee et al. 2010](#), who found that their α -enhanced models are 0.35 mag brighter than the solar-scaled models in the I band. A caveat has to be taken into account at this point as the R and I band spectral regions, and in general the wavelength interval around 7000 Å, are heavily affected by correlation effects. In fact, the $F814W$ band shows the largest differences between spectroscopic and photometric SBF magnitudes at the solar and super-solar metallicity regimes, as clearly shown in Fig. A1 and Fig. 4. Therefore the expected brightening of the SBF due to the consideration of α -elements abundances might not be sufficient to be able to match the empirical calibrations.

Recently, [Cantiello et al. \(2018\)](#) used MegaCam/CFHT imaging of the Virgo cluster to measure SBF distances and provided multiple calibrations of the SBF absolute magnitude in the i -band for different colour combinations. In Fig. 8 and Fig. 9, we plot the absolute SBF magnitudes in the MegaCam/CFHT i -band as a function of the $g - i$ colour, for the same models described above. The calibration (black line)⁹ and data (grey diamonds) for galaxies in the Virgo cluster taken from [Cantiello et al. \(2018\)](#) are also plotted. Note that the calibration in [Cantiello et al. \(2018\)](#) extends to bluer colours than the [Blakeslee et al. \(2010\)](#) one. Regarding the behaviour of SBF magnitudes at lower metallicities, [Blakeslee et al. \(2009\)](#) found that the scatter in their empirical calibration increased at the bluest colours (see also [Cantiello et al. 2018](#)). The fluctuation magnitude measurements in a sample of 25 dwarf spheroidal galaxies in the Fornax cluster obtained by [Mieske, Hilker & Infante \(2006\)](#) yielded a cosmic scatter of 0.34 mag. This scatter is significantly larger than that found at redder colours. This is consistent with what we find for our models at $[\text{Fe}/\text{H}] < -1$, where the values of the SBF absolute magnitude are not uniquely defined with respect to their integrated colours. This scatter might be driven by the presence of stellar populations with different metallicities and ages (in [Cantiello et al. 2018](#) most of the galaxies at $g - i < 0.9$ are late-type). See also the discussion in [Trujillo et al. \(2019\)](#) for the case of an ultra diffuse galaxy and [Carlsten et al. \(2019\)](#) for satellite galaxy systems. Indeed, it has already been suggested that in order to explore SBF calibrations at bluer colours it is necessary to use nonlinear calibrations involving multiple colours (e.g. [Blakeslee et al. 2009](#); [Cantiello et al. 2018](#)).

Our spectroscopic SBF magnitudes are able to match fairly well the empirical SBF distance calibrations, within their validity range. The advantage of using theoretical SBF calibrations is that they are less time consuming to derive,

⁹ The empirical calibration derived in [Cantiello et al. \(2018\)](#) is derived using a subsample of the data.

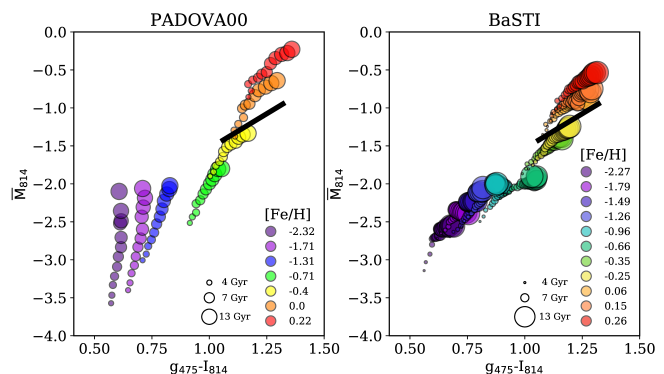


Figure 7. Absolute fluctuation (AB) magnitude in the $F814W$ ACS/HST filter vs. the $g_{475}-I_{814}$ colour. The thick black line shows the calibration of Blakeslee et al. (2010) (their Eq. 2) within its validity range. The filled circles show our model predictions based on the Padova00 (left panel) and BaSTI (right panel) stellar models, computed with bimodal IMF with slope 1.3. The metallicity is varied according to the colour-coding quoted in the bottom right side of the panel, while the sizes of the circles increase with age.

homogeneous in different bands and they make SBF distances a primary distance indicator as they do not rely on Cepheids distances as a zero point. We remark here that deriving SBF based distances with precision require more accurate procedures than the tests performed here. However our SBF spectra are promising and have a potential in aiding these studies based on very precise photometric fluctuation magnitudes.

Finally, we would like to emphasize the utility of the SBF spectra synthesized here to transform between different photometric filter definitions and systems employed for the distance measurements shown here. Moreover, with these models it is possible to achieve more precise comparisons with fluctuation magnitudes and colours measured at varying recession velocities.

6.2 Disentangling relevant stellar population parameters: metal-poor contributions

Given their connection to the properties of the stellar population, SBFs provide additional information on the formation scenarios of galaxies. Fluctuation magnitudes and colours have been used previously to constrain relevant stellar population parameters (e.g., [Liu et al. 2000](#)). To illustrate a possible application of these new models, we compare our fluctuation colour-colour predictions, as derived from the newly synthesized model spectra, with data of a representative set of early-type galaxies, taken from [Blakeslee et al. \(2001\)](#). Such fluctuation colour-colour diagrams were already employed by other authors (e.g., [Liu et al. 2000](#); [Blakeslee et al. 2001](#)), but its use have been hindered by the small number of SBF measurements for varying filter bands in the same galaxies. The SBF spectra computed here provide a flexible way to obtain spectroscopic magnitudes that match observations obtained with any filter/system. We follow the approach described in Section 4.2 to obtain the fluctuation colours that match the observational setup.

Figure 10 shows the $I - K$ vs. $V - I$ fluctuation colour-colour diagram, with a set of representative ETGs

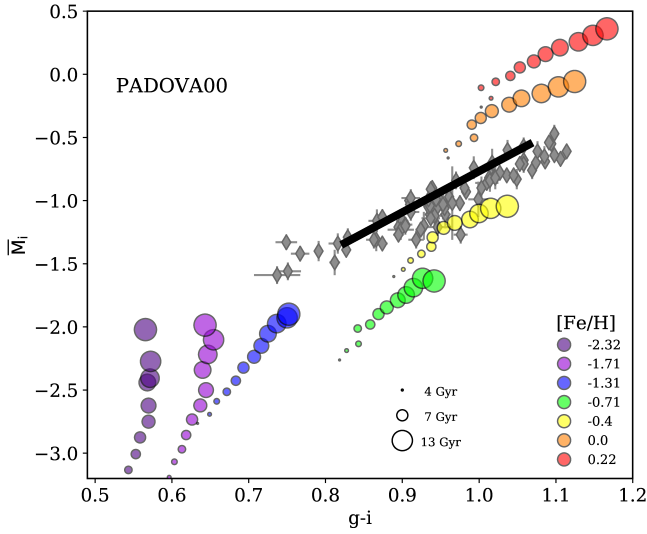


Figure 8. Absolute i band fluctuation as a function of the $g-i$ colour. Both galaxy points (shown in grey) and the calibration within its validity range (thick black line) are taken from [Cantiello et al. \(2018\)](#). The filled circles show our model predictions adopting a bimodal IMF with slope 1.3 and Padova00 stellar models. The metallicity is varied according to the colour-coding quoted in the bottom right side of the panel, while the sizes of the circles increase with age.

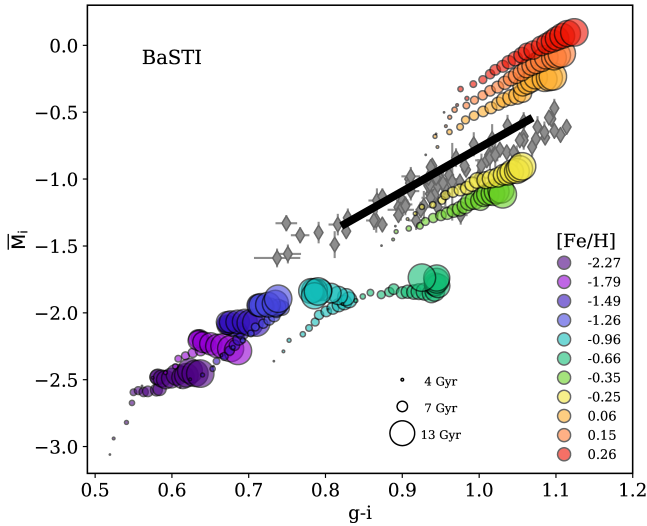


Figure 9. Same as Fig. 8 but for the models computed with the BaSTI isochrones.

(black open squares). The V galaxy data are from [Tonry et al. \(1990\)](#) and [Blakeslee et al. \(2001\)](#), the I data are from [Blakeslee et al. \(1999\)](#); the K data are from [Luppino & Tonry \(1993\)](#) (two galaxies), [Jensen et al. \(1998\)](#) (10 galaxies) and [Pahre & Mould \(1994\)](#) (one galaxy). The plotted single-burst SBF predictions cover a range of metallicities ($-1.79 < [M/H] < 0.26$) and ages above 4 Gyr. We show the predictions for a standard "bimodal" IMF with

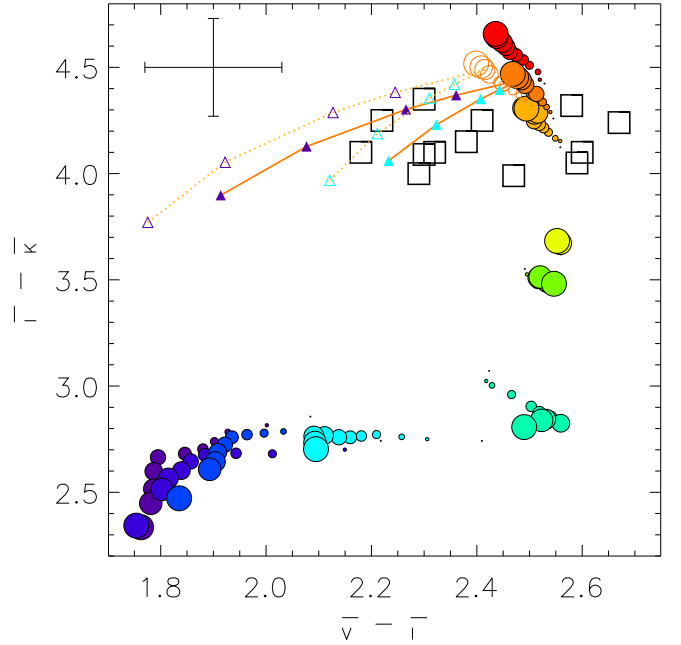


Figure 10. The $I-K$ fluctuation colour is plotted against $V-I$ fluctuation colour (Vega system) for a set of representative ETGs (black open squares with the mean error bars shown on the top left corner; see the text for the sources). Single-burst models (filled circles) of increasing size, which represent an age increase from 4 to 14 Gyr, are shown for each metallicity, $[M/H] = -1.79, -1.49, -1.26, -0.96, -0.66, -0.35, -0.25, +0.06, +0.15$ and $+0.26$, from blue-purple to red, respectively, which are easily distinguished by the various model loci. We adopt a standard "bimodal" IMF with logarithmic slope 1.3 for the upper-segment (above $0.6 M_{\odot}$). For models with $[M/H] = 0.15$ we also show the predictions for a bottom-heavy bimodal IMF with slope 2.8 (open orange circles). In addition, we show composite populations made with a dominant metal-rich component, $[M/H] = 0.15$, with increasing mass-fractions (1, 2, 5 and 10%) of a rather metal-poor component ($[M/H] = -1.79$ blue-purple filled triangles and $[M/H] = -0.96$ in cyan filled triangles). Similar combinations are shown for a bottom-heavy IMF (open triangles with the same colour criterion). These combinations are joined by an orange solid line (standard IMF) or dotted line (bottom-heavy IMF). In all cases the mass-fraction of the metal-poor component increases from redder to bluer $V-I$ fluctuation colour, with these lines starting from the SSP value, i.e. a nil contribution from a metal-poor population.

logarithmic upper-segment slope 1.3 (above $0.6 M_{\odot}$), but we also show some predictions with a bottom-heavy bimodal IMF with slope 2.8 for models with $[M/H] = +0.15$ (open orange circles). This choice of IMF is motivated by recent claims suggesting such dwarf-enriched IMFs in the central regions of massive elliptical galaxies (e.g., [La Barbera et al. 2013](#); [Martín-Navarro et al. 2015](#)). We see that the data fall in a region that is not matched by the models, which seem to loop to around the observational data, with a mean $V-I$ fluctuation value around ~ 2.4 . The single-burst SBF values only approach those galaxies with $V-I$ fluctuation colour above 2.4 (within the error bars). However M 32, with the reddest value, seems to require stellar populations with ages below 4 Gyr, in good agreement with the detailed analysis of its mean spectrum ([Rose et al. 2005](#)). Varying the IMF

shifts the SSP values by ~ 0.05 mag in the correct direction, i.e. along the $V-I$ fluctuation axis as indicated by the open orange circles, with no significant change in the $I-K$ fluctuation axis. However the galaxies with $V-I$ fluctuation value smaller than ~ 2.3 remain clearly out of the reach of the model $V-I$ fluctuation values.

Although not shown we also tested whether the fluctuation colours corresponding to younger (< 4 Gyr) SSPs would be able to match the observed galaxy values. We did not find any single model that could reproduce the galaxies with the bluest $V-I$ fluctuation colours, except for a very few models with $[M/H] = -0.35$ and $[M/H] = -0.25$, which provide $V-I$ fluctuation values that approached a fluctuation colour value of ~ 2.3 . However these contributions would have a large impact on the mean optical galaxy spectrum, such as, e.g., strengthening the Balmer lines, that would not match the observations. A full fitting that comprises varying fractions of components with different ages and metallicities is out of the scope of this work. However we emphasize here the great advantage of using in the analysis both the mean and the SBF spectrum to be able to properly constrain the inferred solutions.

The model loci in Fig. 10 strongly favour the presence of some contributions from fairly metal-poor stellar populations. Therefore we investigate the effects of varying mass fraction contributions from a metal-poor component on top of a dominant metal-rich population. For this purpose we combine an old population of 12 Gyr and slightly super-solar metallicity ($[M/H] = +0.15$) with varying mass-fractions (from 1 to 10%) of a similarly old component with two different metallicity values -1.79 (blue-purple triangles) and -0.96 (cyan triangles). The models including the component with -1.79 require mass-fractions around $\sim 1 - 2\%$ on the top of a vastly dominant super-solar stellar population with a bottom-heavy IMF (open triangles), and $\sim 2 - 4\%$ with a standard IMF (filled triangles). If the metallicity of the metal-poor component is $[M/H] = -0.96$ we obtain mass-fractions as high as 10% when the IMF is standard. We also note that the derived mass fractions for the metal-poor component are not significantly different when we adopt solar metallicity for the dominant stellar population. This is not surprising given the fact that the SSP models of this metallicity provide $V-I$ fluctuation colour values that are close to the super-solar ones.

We have shown that this approach, based on the fluctuation colours, is able to disentangle contributions from very metal-poor components. However this analysis is not completely free from degeneracies as there are varying combinations of stellar populations leading to the same results. In summary, we find that the obtained results depend mostly on the adopted metallicity for the metal-poor component, leading to mass-fractions that can be almost a factor ~ 10 times larger. Note that we have assumed simple models composed of two populations, one old metal-rich to represent the overwhelming dominating contribution and the other one for the very metal-poor, also old, component that characterizes the stellar populations formed during a rapid chemical enrichment that took place before reaching the peak of formation (Vazdekis et al. 1996, 1997). Therefore the larger (smaller) mass-fractions derived when adopting less (more) extreme low metallicities is indicative of a distribution in metallicity that represents that initial enrichment stage. Al-

though out of the scope of this paper we envisage that a more realistic model description for this phase will likely provide a more robust cumulative mass fraction for this metal-poor component. We emphasize that these mass fraction estimates must be taken as an upper limit as our models do not incorporate Post-AGB star spectra that, unlike in the mean SSP spectra, raise the flux of the SBF spectra blueward ~ 3000 Å. This is shown in Fig. 6 for the models of Buzzoni (1989). However such contribution has virtually a negligible impact on the optical range and particularly for the $V-I$ fluctuation colour employed in Fig. 10.

Finally, we also find that when changing the adopted IMF for the dominant component, this fraction varies by a factor of ~ 2 . Finally, the age of the dominant population has little impact on the derived fractions. Additional constraints can be obtained if combined with the analysis of the mean stellar populations properties such as line-strength indices and high resolution spectra.

Our purpose here is to show the potential of the SBF analysis to separate these small contributions, which warrants further research to provide more constrained quantitative estimates. It is worth mentioning that such metal-poor contributions are very difficult to constrain from the standard analysis based on the mean-SSP spectra as a young contribution has a similar effect on the Balmer line indices as the old metal-poor component (e.g., Maraston & Thomas 2000). The mass-fractions derived here are in rather good agreement with the full chemo-evolutionary theoretical predictions of Vazdekis et al. (1997). According to these models, such metal-poor fractions come from the early stages of galaxy evolution during a rapid chemical enrichment phase. Note that such models were able to fit a large variety of colours and line-strength indices of massive ETGs under the assumption of a closed box modelling approach, i.e. fully in-situ formation process.

A significant step further can be achieved by analyzing galaxy SBF spectra, as has been recently attempted by Mitzkus et al. (2018). In Fig. 11 we illustrate this by showing an SBF spectrum corresponding to a single SSP with old age and super-solar metallicity, as typically found for massive elliptical galaxies through a standard spectral analysis, and the SBF spectrum corresponding to a representative solution in the colour-colour fluctuations diagram shown in Fig. 10. The latter model is composed of an old super-solar SSP with a 2% mass-fraction contribution from a population with metallicity $[M/H] = -1.79$ and similar age. The impact of this contribution is barely detected redward the I band, but becomes very strong in the U band, leading to a ~ 1 mag difference with respect to the magnitude of the largely dominant old metal-rich population alone. Note that this capability of the SBF spectra to recover such small fractions of very metal-poor contributions is not related to the age-metallicity degeneracy affecting the mean spectra, in its classical understanding. This degeneracy refers to the overwhelming dominant old metal-rich component that can either be more metal-rich and younger or the other way around to be able to match the observed mean colours.

Another interesting result is the significant flattening of the SBF spectrum shape in the V and R bands, which is responsible for the blueing of the $V-I$ fluctuation colour in Fig. 10. In contrast, the impact of this metal-poor contribution is almost negligible in the mean spectra correspond-

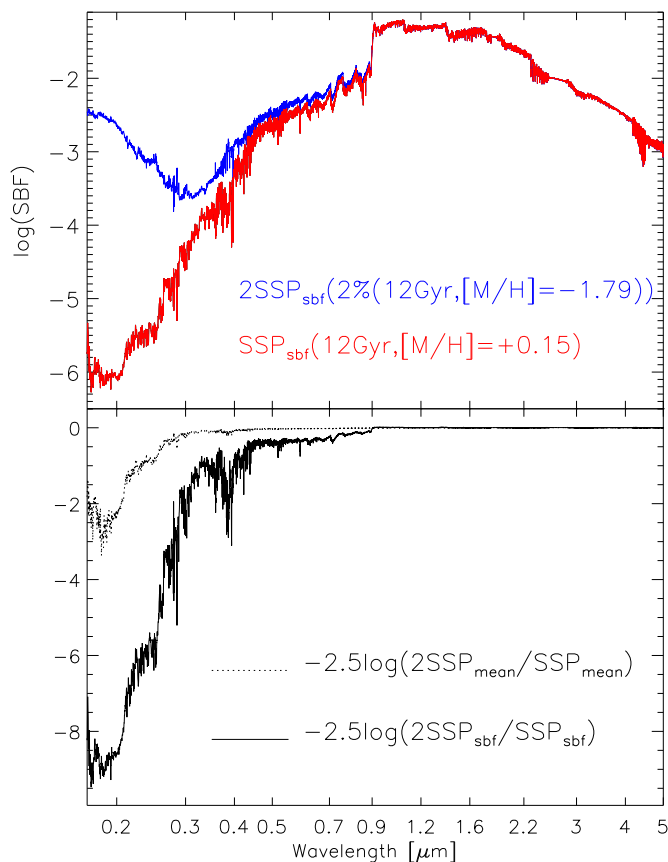


Figure 11. The upper panel shows the SBF spectrum corresponding to an SSP with age 12 Gyr and super-solar metallicity $[M/H] = +0.15$ (plotted in red). Also shown is a representative solution for the colour-colour fluctuations diagram of Fig. 10 (plotted in blue), namely, the composition of that old super-solar SSP with a 2% mass-fraction contribution from a population with metallicity $[M/H] = -1.79$ and similar age. The lower panel shows the difference in magnitudes between these two SBF models (solid black line) and their corresponding mean models (dotted black).

ing to the combined population, being smaller than 0.1 mag redward $\sim 3000 \text{ \AA}$. We also see that the impact of the metal-poor contribution in the UV spectral range is extremely significant, leading to a difference that becomes as large as ~ 8 mag around $\sim 2000 \text{ \AA}$. In this spectral range the effect of this metal-poor component in the corresponding mean SSP spectra is also relevant, reaching ~ 2 mag. However, it would be very difficult to separate these components on the basis of the mean stellar population spectra, as the NUV is also sensitive to tiny contributions from rather young populations (Vazdekis et al. 2016; Salvador-Rusiñol et al. 2019).

Finally, although not shown, we obtain similar residuals to those shown in the lower panel of Fig. 11 for other representative solutions, such as that with a 5% mass-fraction contribution of a population with metallicity $[M/H] = -0.96$. In a more realistic case it is expected that galaxies include such small contributions for a range in metallicities with $[M/H] < -1$. In this case the net mass fraction corresponding to these populations cannot exceed significantly that of a

single population with $[M/H] = -0.96$, i.e. $\sim 10\%$ as inferred from Fig. 10.

6.3 Narrow filter SBF SEDs

We envisage a rather promising potential application of the SBF spectra computed in this work for galaxy surveys that are based on narrow-band filters. As was discussed in Section 4.2, the spectroscopic magnitudes obtained from the theoretical spectra are more accurate for box-shaped transmission responses, preferably, for narrower filters. Such filter systems provide data which lies somewhere between traditional imaging and spectroscopy, and the resulting SEDs are generally characterized by a high photometric precision.

To illustrate such applications we show in Fig. 12 a representative theoretical SBF SED obtained with the narrow filter systems of the Advanced Large, Homogeneous Area Medium Band Redshift Astronomical Survey (ALHAMBRA) at CALAR ALTO observatory (Moles et al. 2008) and the Javalambre Physics of the Accelerating Universe Astrophysical Survey (J-PAS: Benítez et al. 2009; Cenarro et al. 2010). The ALHAMBRA survey is primarily intended for cosmic evolution studies covering a large-area with 20 contiguous, equal width, medium band optical filters from 3500 Å to 9700 Å, and three standard broad bands, JHK, in the NIR (Aparicio-Villegas et al. 2010). The J-PAS survey is based on 56 narrow-band ($\sim 100 \text{ \AA}$) contiguous optical filters ($\lambda \sim 3500 - 9500 \text{ \AA}$) and will be soon providing low resolution ($R \sim 30$) spectro-photometric data for approximately one hundred million galaxies.

The SBF SEDs in Fig. 12 show that these filters not only provide valuable information related to the overall shape of the SED, but have also the ability of measuring the strengths of prominent molecular absorption bands, particularly for the J-PAS survey. This warrants further investigations in order to untangle the information encoded in these features to constrain relevant stellar population parameters. Indeed, given the fact that the SBFs are contributed by the most luminous evolved cool stars, which dominate the light of the mean stellar population SEDs in the near-IR wavelengths, the constraints derived from these stars should also be present in the optical spectral range of the SBF SEDs. Thus, the joint study of the mean and SBF SEDs in the optical range allows us to also include constraints present in the near-IR range of the mean stellar population SED.

7 SUMMARY

Detailed stellar population studies of galaxies are based on fitting their observed spectra and absorption line-strength indices with the aid of theoretical model predictions. The most simple modelling approach is to provide single-age, single-metallicity stellar populations, SSPs, which can be understood as probability distributions that are mainly characterized by mean and variance spectra. In the standard analysis the variance spectra are usually neglected and, consequently, this wastes valuable information that is potentially useful to constrain the SFH. Here we present Surface Brightness Fluctuation spectra computed with the E-MILES stellar population synthesis models. The models cover the spectral range $\lambda \lambda 1680 - 50000 \text{ \AA}$ at moderately high resolution, all

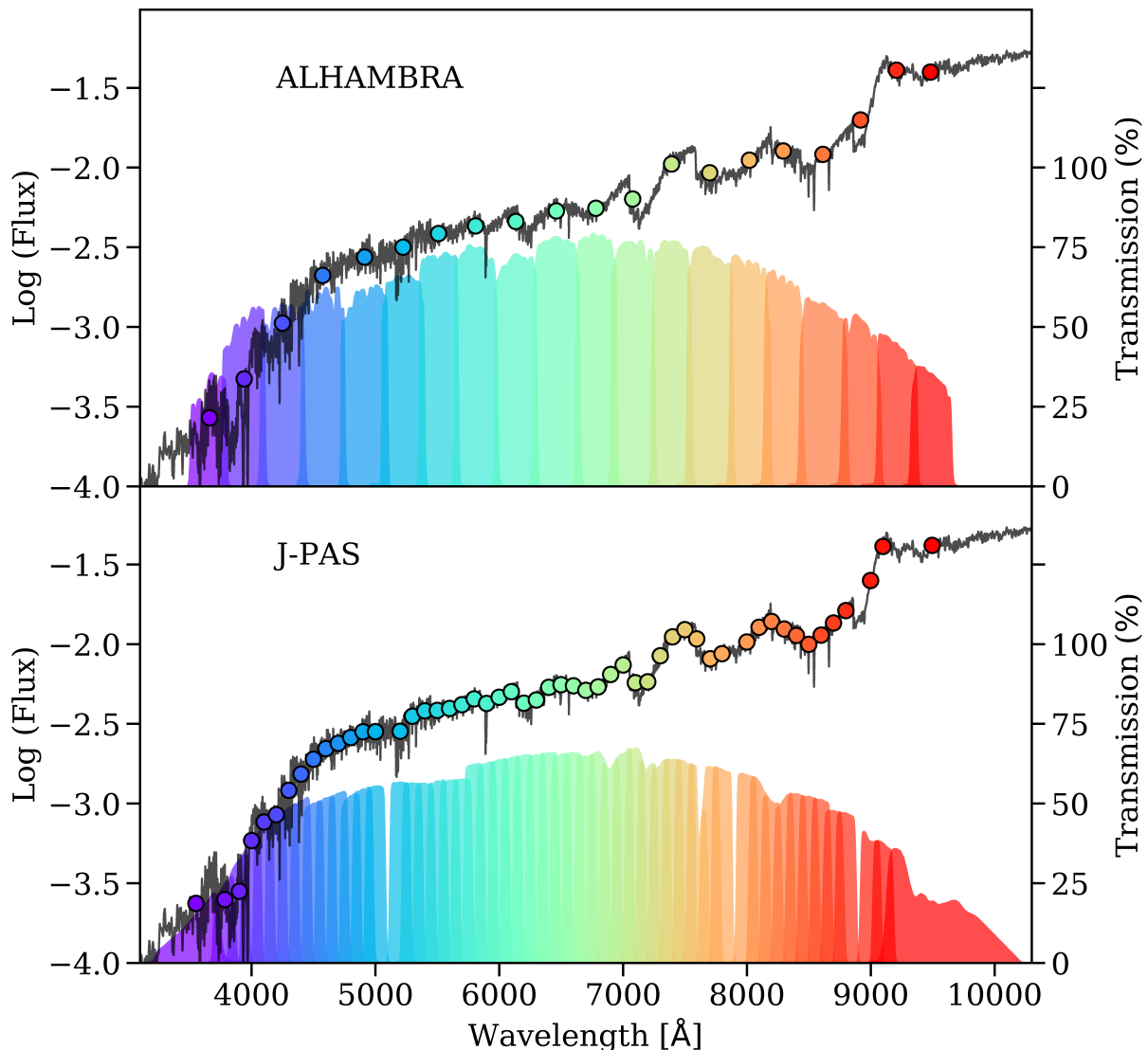


Figure 12. The top panel shows the spectral range of the ALHAMBRA survey at CALAR ALTO showing the narrow filters overplotted on a model SBF spectrum of 10 Gyr and solar metallicity computed with a Kroupa Universal IMF, which is representative of ETGs. The bottom panel shows the filter system of the OAJ/J-PAS survey, which is composed of 56 narrow-band filters.

based on extensive empirical, rather than theoretical, stellar spectral libraries. The models span the metallicity range $-2.3 \leq [M/H] \leq +0.26$ for a suite of IMF types and varying slopes.

Among the main features that distinguish the SBF spectrum from the corresponding mean spectrum we highlight that the flux of the SBF spectrum peaks at much redder wavelengths for old stellar populations (*J,H* bands in the SBF spectrum and *V,R* bands in the mean spectrum). Another remarkable feature of the SBF spectrum is that it shows much stronger molecular band absorption, which can erase to a great extent prominent features in the mean spectrum such as the CaII triplet in the *I* band. We have characterized the impact of the stellar evolutionary models that feed our stellar population models on the resulting SBF spectra. As expected, the impact on the SBF spectra is much larger due to the significant contribution of the

later evolutionary stages on the resulting models. We have characterized the behaviour of the SBF spectra with varying stellar population parameters, i.e., age, metallicity and IMF. We find that the SBF spectra are mostly sensitive to age and metallicity, providing further constraints on the stellar content inferred from the standard analysis based on the mean spectra. We also have studied the behaviour of the SBF spectra with varying α -enhancement. At constant total metallicity the abundance enhanced SBF spectra are brighter by 0.1 – 0.2 mag in the optical range whereas, at constant iron abundance, the α -enhanced SBF spectra are fainter by 0.3 – 0.4 mag.

We discuss the possible use of the SBF spectra in some practical cases. Due to the properties of the variance, the construction of the SBF spectrum corresponding to a SFH has to be made by combining the variances and the mean spectra of the various SSP components separately. These

are then divided to obtain the combined SBF spectrum. We also test several approaches to obtain spectroscopic fluctuation magnitudes from the SBF spectra. The best results are obtained by adopting the hypothesis of full correlation within the filter wavelength domain. Note that such approach provides the brightest possible magnitudes. We have compared these spectroscopic magnitudes to the photometric ones, which are computed in the standard way on the basis of extensive stellar photometric libraries. This comparison provided us with offsets, due to non full correlation within the filter wavelength domain, which can be used to correct the spectroscopic magnitudes. We tabulate these offsets for a variety of widely used set of filters and provide a detailed recipe for measuring the spectroscopic SBF magnitudes, provided the variance and mean spectra.

We compare our models with those of various authors, which employ stellar isochrones and stellar libraries that differ from the empirical ones that feed our models. The recently published SBF model spectra of [Mitzkus et al. \(2018\)](#) are in reasonably good agreement with our predictions, the two based on the MILES stellar spectral library. These comparisons highlighted a striking difference that is caused by Post-AGB stars and white dwarf evolution, only included in the [Buzzoni \(1989\)](#) models, which increase the flux of the SBF spectra blueward ~ 3000 Å. Such contributions are extremely significant in the NUV range in the SBF spectra, whereas their impact on the mean spectra is only detectable in the FUV. Such sensitivity can be potentially used to study the UV upturn phenomenon present in a fraction of elliptical galaxies.

Although high quality photometric SBF magnitudes are required for a variety of studies, we show that the spectroscopic SBF magnitudes can be also useful at aiding and complement these studies. The SBF spectra can be used to generate fluctuation magnitudes for a variety of situations in a rather easy way. The SBF model spectra can be also useful to transform between varying definitions of a given photometric filter, or to achieve precise comparisons with fluctuation magnitudes and colours from varying sources. We compare our spectroscopic fluctuation magnitudes with empirical SBF calibrations that are used for distance measurements and find a reasonably good agreement.

The SBF spectra are very useful to constrain relevant stellar population parameters. In fact, by comparing the predicted SBF spectra to a representative sample of ETGs we untangle small ($< 5\%$) mass-fraction contributions from extremely metal-poor ($[M/H] < -1$) components. This result is particularly remarkable, given the strong insensitivity of the standard spectral analysis to these small contributions of very metal-poor stellar populations in the visible and in the near-IR spectral ranges, which are completely hidden by the dominant, old metal-rich, stellar population. Thus, SBF spectra have the potential to put very stringent constraints on the early stages of the formation of the ETGs. These results should motivate new observations and the use of catalogues of multi-wavelength SBF measurements of large sample of galaxies such as, e.g., the Next Generation Virgo Cluster Survey ([Cantiello et al. 2018](#)).

Finally, we also show that the new SBF models represent an excellent opportunity for exploiting ongoing photometric surveys, particularly those based on narrow-band filters. However, significant modelling work is ur-

gently required to identify and characterize those spectrophotometric features that provide the most relevant constraints. These new models can be downloaded from the MILES website (<http://miles.iac.es/>).

ACKNOWLEDGMENTS

We thank M. Mitzkus and C. J. Walcher for kindly providing us with a set of their recently published SBF model spectra. We are very grateful to the referee who provided a very constructive and detailed comments and suggestions that helped us to improve significantly the original draft. We thank P. Rodríguez-Beltrán and J. Falcón-Barroso for preparing the model distribution for the miles website. We are grateful to I. Trujillo and G. van de Venn for very useful discussions. AV thanks the ESO visitor program support (2018). This work has been supported by the grants AYA2016-77237-C3-1-P, AYA2017-88007-C3-1-P, AYA2015-68012-C2-01 and MDM-2017-0737 (Unidad de Excelencia María de Maeztu CAB) from the Spanish Ministry of Science, Innovation and Universities (MCIU). This work has been supported through the regional budget of the Consejería de Economía, Industria, Comercio y Conocimiento of the Canary Islands Autonomous Community. MB gratefully acknowledges support from the Severo Ochoa excellence programme (SEV-2015-0548). IMN acknowledges support from the Marie Skłodowska-Curie Individual *SPanD* Fellowship 702607.

REFERENCES

- Alonso, A., Arribas, S., Martínez-Roger, C., 1995, *A&A*, 297, 197
- Alonso, A., Arribas, S., Martínez-Roger, C., 1996, *A&A*, 313, 873
- Alonso, A., Arribas, S., Martínez-Roger, C., 1999, *A&AS*, 140, 261
- Aparicio-Villegas, T., et al., 2010, *AJ*, 139, 1242
- Benítez, N., et al., 2009, *ApJ*, 691, 241
- Bessell, M. S., Brett, J. M., Wood, P. R., Scholz, M., 1989, *A&AS*, 77, 1
- Bessell, M. S., Brett, J. M., Scholz, M., Wood, P. R., 1991, *A&AS*, 89, 335
- Blakeslee, J. P., Davis, M., Tonry, J. L., Dressler, A., Ajhar, E. A., 1999, *ApJ*, 527, L73
- Blakeslee, J. P., Vazdekis, A., Ajhar, E. A., 2001, *MNRAS*, 320, 193
- Blakeslee, J. P., Jordán, A., Mei, S., Côté, P., Ferrarese, L., Infante, L., Peng, E. W., Tonry, J. L., West, M. J., 2009, *ApJ*, 694, 556
- Blakeslee, J. P., Cantiello, M., Mei, S., et al., 2010, *ApJ*, 724, 657
- Blakeslee, J. P., 2010, *Ap&SS*, 341, 179
- Bressan, A., Marigo, P., Girardi, L., Salasnich, B., Dal Cero, C., Rubele, S., Nanni, A., 2012, *MNRAS*, 427, 127
- Buser, R., Kurucz, R. L., 1978, *A&A*, 70, 555
- Buzzoni, A. 1989, *ApJS*, 71, 817
- Buzzoni, A. 1993, *A&A*, 275, 433
- Buzzoni, A. 2005, in *Resolved Stellar Populations* IAU symp. (unpublished) [arXiv:astro-ph/0509602](https://arxiv.org/abs/astro-ph/0509602)
- Caffau, E., Ludwig, H.-G., Steffen, M., Freytag, B., Bonifacio, P., 2011, *Sol. Phys.*, 268, 255
- Cantiello, M., Raimondo, G., Brocato, E., Capaccioli, M., 2003, *AJ*, 125, 2783
- Cantiello, M., Blakeslee, J. P., Raimondo, G., Mei, S., Brocato, E., Capaccioli, M., 2005, *ApJ*, 634, 239

- Cantiello, M., Blakeslee, J., Raimondo, G., Brocato, E., Capaccioli, M., 2007, *ApJ*, 668, 130
- Cantiello, M., Brocato, E., Capaccioli, M., 2011, *A&A*, 534, 35
- Cantiello, M., Blakeslee, J. P., Ferrarese, L., Côté, P., Roediger, J. C., Raimondo, G., Peng, E. W., Gwyn, S., Durrell, P. R., Cuillandre, J.-C., 2018, *ApJ*, 856, 126
- Carlsten, S. G., Beaton, R. L., Greco, J. P., Greene, J. E., 2019, *ApJ*, 878, L16
- Cassisi, S., Castellani, V., Ciarcelluti, P., Piotto, G., Zoccali, M., 2000, *MNRAS*, 315, 679
- Cassisi, S., Salaris, M., Castelli, F., Pietrinferni, A., 2004, *ApJ*, 616, 498
- Cenarro, A. J., Cardiel, N., Gorgas, J., Peletier, R. F., Vazdekis, A., Prada, F., 2001a, *MNRAS*, 326, 959
- Cenarro, A. J., Gorgas, J., Cardiel, N., Pedraz, S., Peletier, R. F., Vazdekis, A., 2001b, *MNRAS*, 326, 981
- Cenarro, A. J., et al., 2007a, *MNRAS*, 374, 664
- Cenarro, A. J., Moles, M., Cristóbal-Hornillos, D., Gruel, N., Benítez, N., Marín-Franch, A., 2010, *SPIE*, 7738
- Cerviño, M. 2013, *New Astron. Rev.*, 57, 123
- Cerviño, M., & Luridiana, V. 2006, *A&A*, 451, 475
- Cerviño, M., Luridiana, V., & Jamet, L. 2008, *A&A*, 491, 693
- Cerviño, M., & Luridiana, V. 2009, *New Quests in Stellar Astrophysics. II. Ultraviolet Properties of Evolved Stellar Populations*, 293
- Cerviño M., Valls-Gabaud D., 2003, *MNRAS*, 338, 481
- Chabrier, G., 2001, *ApJ*, 554, 1274
- Chabrier, G., 2003, *PASP*, 115, 763
- Coelho P. R. T., 2014, *MNRAS*, 440, 1027
- Coelho, P., Barbuy, B., Melendez, J., Schiavon, R., Castilho, B., 2005, *A&A*, 443, 735
- Coelho, P., Bruzual, G., Charlot, S., Weiss, A., Barbuy, B., Ferguson, J. W., 2007, *MNRAS*, 382, 498
- Cordier, D., Pietrinferni, A., Cassisi, S., Salaris, M., 2007, *AJ*, 133, 468
- Cushing, M. C., Raynier, J. T., Vacca, W. D., 2005, *ApJ*, 623, 1115
- Falcón-Barroso, J., Sánchez-Blázquez, P., Vazdekis, A., Ricciardelli, E., Cardiel, N., Cenarro, A. J., Gorgas, J., Peletier, R. F., 2011, *A&A*, 532, 95
- Fluks, M. A., Plez, B., Thé, P. S., de Winter, D., Westerlund, B. E., Steenman, H. C., 1994, *A&AS*, 105, 311
- Fukugita, M., Shimasaku, K., Ichikawa, T., 1995, *PASP*, 107, 945
- Girardi, L., Bressan, A., Bertelli, G., Chiosi, C., 2000, *A&AS*, 141, 371
- González Delgado, R. M., Cerviño, M., Martins, L. P., Leitherer, C., & Hauschildt, P. H. 2005, *MNRAS*, 357, 945
- González, R. A., Liu, M. C., & Bruzual A., G. 2004, *ApJ*, 611, 270
- González-Lópezlira R. A., Bruzual-A. G., Charlot S., Ballesteros-Paredes J., Loinard L., 2010, *MNRAS*, 403, 1213
- González-Lópezlira R. A., 2018, *ApJ*, 856, 170
- Gregg, M. D., Silva, D., Rayner, J., et al. 2006, in *The 2005 HST Calibration Workshop: Hubble After the Transition to Two-Gyro Mode*, ed. A. M. Koekemoer, P. Goudfrooij, & L. L. Dressel, 209–215
- Grevesse, N., Sauval, A. J., 1998, *Space Sci. Rev.*, 85, 161
- Hayes, D. S., 1985, in D. S. Hayes, L. E. Pasinetti, & A. G. D. Philip, eds. *Proc. IAU Symposium 111, Calibration of fundamental stellar quantities*. Dordrecht, Reidel, p., 225.
- Jacoby G. H., et al., 1992, *PASP*, 104, 599
- Jensen, J. B., Tonry, J. L., Luppino G. A., 1998, *ApJ*, 505, 111
- Jensen, J. B., Tonry, J. L., Thompson, R. I., Ajhar, E. A., Lauer, T. R., Rieke, M. J., Postman, M., Liu, M. C., 2001, *ApJ*, 550, 503
- Jensen, J. B., Tonry, J. L., Barris, B. J., Thompson, R. I., Liu, M. C., Rieke, M. J., Ajhar, E. A., Blakeslee, J. P., 2003, *ApJ*, 583, 712
- Jensen, J. B., Blakeslee, J. P., Gibson, Z., Lee, H.-C., Cantiello, M., Raimondo, G., Boyer, N., Cho, H., 2015, *ApJ*, 808, 91
- Koleva, M., Vazdekis, A., 2012, *A&A*, 538, 143
- Kroupa, P., 2001, *MNRAS*, 322, 231
- La Barbera, F., Ferreras, I., Vazdekis, A., de la Rosa, I. G., de Carvalho, R. R. Trevisan, M., Falcón-Barroso, J., Ricciardelli, E., 2013, *MNRAS*, 433, 3017
- Lee, H.-C., Worthey, G., Blakeslee, J. C., 2010, *ApJ*, 710, 421
- Castro-Almazán J. A., Pérez-Jordán G., Muñoz-Tuñón C., 2016, *AMT*, 9, 4759
- Lejeune, T., Cuisinier, F., Buser, R., 1997, *A&AS*, 125, 229
- Lejeune, T., Cuisinier, F., Buser, R., 1998, *A&AS*, 130, 65
- Liu, M. C., Graham, J. R., Charlot, S., 2002, *ApJ*, 564, 216
- Liu, M. C., Charlot, S., Graham, J. R., 2000, *ApJ*, 543, 644
- Luppino, G. A., Tonry, J. L., 1993, *ApJ*, 410, 81
- Maraston, C., Thomas, D., 2000, *ApJ*, 541, 126
- Marigo, P., et al., 2017, *ApJ*, 835, 77
- Marín-Franch, A., & Aparicio, A., 2003, *ApJ*, 594, 63
- Marín-Franch, A., & Aparicio, A., 2006, *A&A*, 450, 979
- Mármol-Queraltó, E., Cardiel, N., Cenarro, A. J., Vazdekis, A., Gorgas, J., Pedraz, S., Peletier, R., Sánchez-Blázquez, P., 2008, *A&A*, 489, 885
- Martín-Navarro, I., La Barbera, F., Vazdekis, A., Falcón-Barroso, J., Ferreras, I., 2015, *MNRAS*, 447, 1033
- Martín-Navarro, I., Vazdekis, A., Falcón-Barroso, J., La Barbera, F., Y0131ld0131r0131m, A., van de Ven, G., 2018, *MNRAS*, 475, 3700
- Martins L. P., González Delgado R. M., Leitherer C., Cerviño M., Hauschildt P., 2005, *MNRAS*, 358, 49
- Mieske, S., Hilker, M., Infante, L., 2006, *A&A*, 458, 1013
- Milone, A. de C., Sansom, A. E., Sánchez-Blázquez, P., 2011, *MNRAS*, 414, 1227
- Mitzkus, M., Jakob Walcher, C. Roth, M. M., Coelho, P. R. T., Cioni, M. R. L., Raimondo, G., Rejkuba, M., 2018, *MNRAS*, 480, 629
- Moles, M., et al., 2008, *AJ*, 136, 1325
- Montes, M., Acosta-Pulido, J. A., Prieto, M. A., Fernández-Ontiveros, J. A., 2014, *MNRAS*, 442, 1350
- Mouhcine, M., González, R. A., Liu, M. C., 2005, *MNRAS*, 362, 1208
- Noël, N. E. D., Greggio, L., Renzini, A., Carollo, C. M., Maraston, C., 2013, *ApJ*, 772, 58
- Pahre, M. A., Mould, J. R., 1994, *ApJ*, 433, 567
- Pietrinferni, A., Cassisi, S., Salaris, M., Castelli, F., 2004, *ApJ*, 612, 168
- Pietrinferni, A., Cassisi, S., Salaris, M., Castelli, F., 2006, *ApJ*, 642, 797
- Pietrinferni, A., Cassisi, S., Salaris, M., Percival, S., Ferguson, J. W., 2013, *ApJ*, 697, 275
- Pietrinferni, A., Cassisi, S., Salaris, M., Hidalgo, S., 2013, *A&A*, 558, 46
- Raimondo, G., 2009, *ApJ*, 700, 1247
- Raimondo, G., Brocato, E., Cantiello, M., & Capaccioli, M. 2005, *AJ*, 130, 2625
- Raynier, J. T., Cushing, M. C., Vacca, W. D., 2009, *ApJS*, 185, 289
- Reimers, D., 1977, *A&A*, 57, 395
- Renzini, A., 2006, *ARAA*, 44, 141
- Renzini, A., Fusi Pecci, F., 1988, *ARAA*, 26, 199
- Ricciardelli, E., Vazdekis, A. Cenarro, A. J., Falcón-Barroso, J., 2012, *MNRAS*, 424, 172
- Röck, B., Vazdekis, A., Peletier, R. F., Knapen, J. H., Falcón-Barroso, J., 2015, *MNRAS*, 449, 2853
- Röck, B., Vazdekis, A., Ricciardelli, E., Peletier, R. F., Knapen, J. H., Falcón-Barroso, J., 2016, *A&A*, 589, 73
- Rose, J. A., Arimoto, N., Caldwell, N., Schiavon, R. P., Vazdekis, A., Yamada, Y., 2005, *AJ*, 129, 712
- Salpeter, E. E., 1955, *ApJ*, 121, 161

- Salvador-Rusiñol, N., Vazdekis, A., La Barbera, F., Beasley, M. A., Ferreras, I., Negri, A., Dalla Vecchia, C., 2019, *Nature Astronomy*, in press.
- Sánchez-Blázquez, P., et al., 2006, *MNRAS*, 371, 703
- Sánchez-Blázquez, P., Duncan, A., Strader, J., Brodie, J., Proctor, R., 2007, *MNRAS*, 377, 759
- Sánchez, S. F., et al., 2012, *A&A*, 538, 8
- Sánchez-Gil M. C., Alfaro E. J., Cerviño M., Pérez E., Bland-Hawthorn J., Jones D. H., 2019, *MNRAS*, 483, 2641
- Sodemann, M., Thomsen, B., 1996, *AJ*, 111, 208
- Sodemann, M., Thomsen, B., 1995, *AJ*, 110, 179
- Spolaor, M., Kobayashi, C., Forbes, D. A., Couch, W. J., Hau, G. K. T., 2010, *MNRAS*, 408, 272
- Tinsley, B. M., 1980, *Fundam. Cosmic Phys.*, 5, 287
- Tonry, J. L., Ajhar, E. A., Luppino, G. A., 1990, *AJ*, 100, 1416
- Tonry J. L., 1991, *ApJ*, 373, L1
- Tonry J. L., Dressler A., Blakeslee J. P., Ajhar E. A., Fletcher A. B., Luppino G. A., Metzger M. R., Moore C. B., 2001, *ApJ*, 546, 681
- Tonry, J., & Schneider, D. P. 1988, *AJ*, 96, 807
- Trujillo, I., et al., 2019, *MNRAS*, 486, 1192
- Valdes, F., Gupta, R., Rose, J. A., Singh, H. P., Bell, D. J., 2004, *ApJS*, 152, 251
- Vazdekis, A., Casuso, E., Peletier, R. F., Beckman, J. E., 1996, *ApJS*, 106, 307
- Vazdekis, A., Peletier, R. F., Beckman, J. E., Casuso, E., 1997, *ApJS*, 111, 203
- Vazdekis, A., Cenarro, A. J., Gorgas, J., Cardiel, N., Peletier, R. F., 2003, *MNRAS*, 340, 1317
- Vazdekis A., Sánchez-Blázquez P., Falcón-Barroso J., Cenarro A. J., Beasley M. A., Cardiel N., Gorgas J., Peletier R. F., 2010, *MNRAS*, 404, 1639)
- Vazdekis, A., Ricciardelli, E., Cenarro, A. J., Rivero-González, J. G., Díaz-García, L. A., Falcón-Barroso, J., 2012, *MNRAS*, 424, 157
- Vazdekis, A., Coelho, P., Cassisi, S., Ricciardelli, E., Falcón-Barroso, J., Sánchez-Blázquez, P., La Barbera, F., Beasley, M., Pietrinferni, A., 2015, *MNRAS*, 449, 1177
- Vazdekis, A., Koleva, M., Ricciardelli, E., Röck, B., Falcón-Barroso, J., 2016, *MNRAS*, 463, 3409
- Westera P., Lejeune T., Buser R., Cuisinier F., Bruzual G., 2002, *A&A*, 381, 524
- Worthey, G., 2004, *AJ*, 128, 2826
- Worthey, G., 1994, *ApJS*, 95, 107
- Yi, S. K., Lee, J., Sheen, Y.-K., Jeong, H., Suh, H., Oh, K., 2011, *ApJS*, 195, 22

APPENDIX A: SPECTROSCOPIC SBF MAGNITUDES AND CORRECTION FACTORS

Users of the SBF spectra could be tempted to perform a direct integration for computing magnitudes or spectral indices. However such an integration, although providing the correct units, would not be able to recover the involved variance properties. Written explicitly, and taking into account the quadratic term in the variance, we obtain the following expressions that are not equivalent

$$\int_{m_1}^{m_2} \left(\int_{\lambda} L_{\lambda}(m, t, [\text{Fe}/\text{H}]) T(\lambda) d\lambda \right)^2 N_{\Phi}(m, t) dm \neq \int_{\lambda} \left(\int_{m_1}^{m_2} L_{\lambda}^2(m, t, [\text{Fe}/\text{H}]) N_{\Phi}(m, t) dm \right) T(\lambda) d\lambda \quad (\text{A1})$$

that is, any property integrated over the wavelength domain

will lead to a different variance when the integration is performed either before or after the computation of the stellar population. It so happens that the different wavelengths in a stellar spectrum are related to each other, and such correlations should be preserved (and propagated) in the computation of the spectrum of a stellar population. This is the case when convolving the SBF spectrum with a given filter response to obtain spectroscopic photometry, or simply, when re-sampling the SBF spectrum to a different resolution.

A proper treatment requires obtaining the correlation matrix between all wavelengths during the computation of the SBF spectrum of the SSP:

$$\int_{m_1}^{m_2} L_{\lambda_i}(m, t, [\text{Fe}/\text{H}]) L_{\lambda_j}(m, t, [\text{Fe}/\text{H}]) N_{\Phi}(m, t) dm \quad \forall i, j \quad (\text{A2})$$

for all the wavelengths in the spectra (with the corresponding subtraction of the product $L_{\lambda_i}^{\text{SSPmean}} L_{\lambda_j}^{\text{SSPmean}}$ to transform it to a covariance) to obtain the corresponding covariance matrix. However in a practical use of the SBF spectrum such a treatment would be cumbersome. Therefore, we have explored various alternative approximations to simplify such complexities. The most simple case is obtained under the assumption of fully correlated spectra, as discussed in the main text (see Section 4.2). In this section we show that such an approach provides the best simple solution for obtaining the spectroscopic SBF photometry, despite its limitations, which include possible issues related to the loss of full correlation in the strongest absorption lines in the SBF spectrum.

We employ here the *SED@* models of Cerviño & Luridiana (2006), with BaSTI and Padova00 isochrones and the low resolution BaSeL3.1 stellar spectral library of Westera et al. (2002), to investigate these alternatives. We derive the spectroscopic fluctuation magnitudes from the computed spectra and we also calculate the photometric magnitudes in the standard way, i.e. integrating over the isochrone the individual star fluxes in the selected band leading to

$$L_{\text{band}}^{\text{SSPsf}}(\text{sf}_{\text{PHOT}}) = \frac{\langle L_{\text{band}}^2 \rangle}{\langle L_{\text{band}} \rangle}. \quad (\text{A3})$$

The models are self-consistent in the sense that the two approaches lead to the same $L_{\text{band}}^{\text{SSPmean}}$ result. Therefore we focus on comparing the results of the various approaches for obtaining $L_{\lambda}^{\text{SSPvar}}$ or $L_{\lambda}^{\text{SSPsf}}$ from their corresponding spectra. The first step consists in establishing the coefficients of integration over the filter T_{λ_i}

$$L_{\text{band}} = \int T(\lambda) L_{\lambda} d\lambda = \sum_{i=1}^N T_{\lambda_i} L_{\lambda_i} \quad (\text{A4})$$

where L_{λ_i} is either the spectrum of an individual star or the mean SSP spectrum, which in this particular case are defined by their resolution.

Having defined T_{λ_i} we now consider four possible alternatives. The first two cases represent the most extreme assumptions regarding the correlation between the different wavelengths, namely, full (positive) correlation ($\rho = 1$, with ρ representing the correlation coefficient) and null correlation ($\rho = 0$), which lead to

$$L_{band}^{SSPvar}(\rho = 1) = \left(\sum_{i=1}^N T_{\lambda_i} \sqrt{L_{\lambda_i}^{SSPvar}} \right)^2 \quad (A5)$$

$$L_{band}^{SSPvar}(\rho = 0) = \sum_{i=1}^N T_{\lambda_i}^2 L_{\lambda_i}^{SSPvar} \quad (A6)$$

The other two cases correspond to the direct integration of the filter profile with the SBF spectrum $L_{band}^{SSPsf}(sf)$, or the variance spectrum $L_{band}^{SSPvar}(var)$

$$L_{band}^{SSPsf}(sf) = \sum_{i=1}^N T_{\lambda_i} L_{\lambda_i}^{SSPsf} \quad (A7)$$

$$L_{band}^{SSPvar}(var) = \sum_{i=1}^N T_{\lambda_i} L_{\lambda_i}^{SSPvar} \quad (A8)$$

It is worth noting that the case of $L_{band}^{SSPsf}(sf)$ is not a mathematically correct approach as it does not allow us to recover the variance within the band. The SBF obtained in this way represents the ratio between the variance and the mean spectra within the photometric band and, consequently, it does not preserve the properties of a variance and a *bona-fide* SBF. Finally, in the last case we add the individual variances weighted by the filter transmission, which resembles the method proposed for the computation of the variance of a Star Formation History. Note that the SFH follows a frequency distribution and, therefore, its use can be justified in the scaling relations of the statistical properties of the stellar populations. However, in the present case neither the transmission curve represents a frequency distribution in the statistical sense, nor can we make use of any scaling relation based on the statistical properties of the spectrum.

We have applied these four approaches to obtain the spectroscopic SBF magnitudes corresponding to a variety of standard filter systems and the two sets of isochrones. We find similar trends for all the filters. We illustrate the results in Fig. A1 for the F814W HST filter. This filter is the that which shows the largest difference between the spectroscopic and photometric magnitudes. The figure shows the ratio of the spectroscopic SBF magnitude obtained with different methods with respect the photometric value and indicates that the fully uncorrelated case is completely out of scale. It strongly underestimates the reference photometric SBF value (note the change of scale between the upper and lower parts of the diagram). The other three cases produce far better results, with the fully correlated case, $L_{band}^{SSPvar}(\rho = 1)$, the one which provides the best results. This approach overestimates slightly the photometric SBF magnitude. We note that, formally, this case represents the maximum allowed overestimation. Finally, the cases in which we apply a direct integration of the filter response over the SBF or the variance spectrum lead to slightly larger overestimates. Their performance depends on the age range regime and the filter. Despite the fact that these two approaches are reasonably straightforward to compute, we discourage their use due to such dependencies on age and filter, and because they do not provide smaller deviations with respect to the photometric magnitudes.

Given these results we select the full correlation wavelength approach to obtain the spectroscopic magnitudes. Figure A1 shows that this method leads to better results

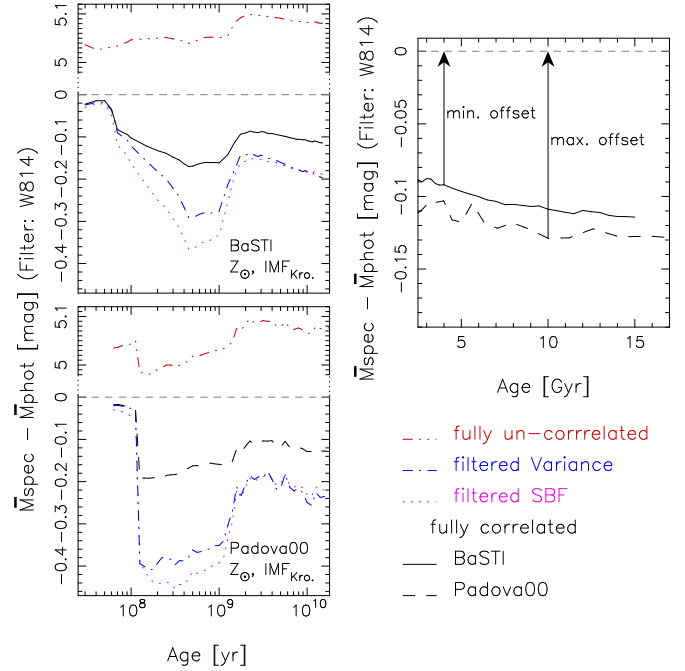


Figure A1. SBF magnitude difference obtained for the F814W filter by comparing the photometric magnitude to the one synthesized from the SBF spectrum using different methods. The results are shown as a function of age for solar metallicity and Kroupa Universal IMF. We selected the F814W filter as it provides the poorest agreement and, therefore, it helps at emphasizing the difference between these varying methods. The left panels represent the results obtained for the models based on the BaSTI isochrones (upper) and Padova00 (lower). Note that there is a scale change between the upper and lower part in these two panels. The solid (top-left panel for BaSTI) and dashed (bottom-left panel for Padova00) black lines represent the spectroscopic SBF magnitudes assuming the hypothesis of full correlation within the filter passband ($L_{band}^{SSPvar}(\rho = 1)$ in the text). The red dotted-dotted-dashed lines in the left panels correspond to the fully uncorrelated case ($L_{band}^{SSPvar}(\rho = 0)$ in the text). The pink dotted lines in the same panels represent the direct application of the filter over the SBF spectrum ($L_{band}^{SSPsf}(sf)$). Finally the blue dashed-dotted lines show the results for a direct application of the filter response over the variance spectrum ($L_{band}^{SSPvar}(var)$). The black thin dashed line represents the perfect match in the left panels. The top-right panel shows the maximum and minimum offsets obtained with the full correlation hypothesis for the two set of isochrones. These values are the ones tabulated in Tables A1, A2 and A3.

at lower ages, where the same massive stars dominate the luminosity in a fairly wide wavelength range. The largest differences are obtained for intermediate ages, specifically between 0.1 and 2 Gyr, where AGB stars maximize their relative contribution to the total light in this spectral range. However, the fraction with which these stars contribute is a strong function of wavelength, leading to a departure from the full correlation hypothesis. Finally for the old age regime, above 2 Gyr the difference in magnitude does not change significantly as a function of age.

Tables A1, A2 and A3 list the maximum and minimum offsets that are required to match the spectroscopic SBF magnitudes to the photometric ones due to non full correlation effects. These limiting values correspond to the absolute

minimum and maximum differences obtained within the age regime older than 4 Gyr (5 Gyr for the metallicity $Z = 0.040$ for the BaSTI isochrones) and by varying the input set of isochrones (Padova00 and BaSTI). These offsets are provided for different metallicity bins. When a metallicity value is missing in one of the two isochrone sets employed here, we interpolate linearly the corresponding minimum and maximum values found for the closest bracketing metallicities that are available. We stress here that such offsets should not be extrapolated to lower ages, as illustrated in the right panel of Fig. A1.

APPENDIX B: ALTERNATIVE ROUTES TO DERIVE OBSERVATIONAL SBF SPECTRA

The use of SBF spectra to constrain relevant stellar population parameters, together with the classical approach based on mean SSP spectra, has been recently tackled by Mitzkus et al. (2018). To obtain the observational SBF spectrum these authors followed the approach of Tonry & Schneider (1988), which is based on a Fourier Transform (FT) analysis. The method is aimed at disentangling the instrumental noise and the SBF signal that is correlated with the Point Spread Function (PSF). Although this approach has proven advantages, it requires PSF-correlated data to work.

It is interesting to explore alternative routes to obtain the SBF spectrum from already existing observations. We mention that proposed by Buzzoni (2005), which is based on the theoretical formulation of the SBF, i.e., without recourse to the PSF and FT analysis. In practise we only require a set of galaxy spectra that allow us to obtain a mean and a variance spectrum. The method depends, however, on the way that the observational spectra have been acquired. It is worth mentioning that it is not our intention here to derive such spectra, but to provide a general outline of the method. We are presently working on developing this approach and present the results elsewhere.

For IFU galaxy data we propose the following procedure:

(i) Select IFU spectra along a given galaxy isophote with good signal to noise ratio, as is usually done in the standard analysis. This choice minimizes possible variations in the number of stars as well as variations of relevant stellar population parameters. Indeed, it is important to recognise that the IMF, SFH, age, metallicity and abundance ratios, are found to vary radially within early-type galaxies (e.g., Martín-Navarro et al. 2018). In other words, it is assumed that each of the selected spectra along the isophote is a particular realization of a generic population with similar physical parameters and that each spectrum is the result of a similar number of stars.

(ii) Use the selected spectra to obtain the average (mean) galaxy isophotal spectrum, $F_{\lambda}^{\text{mean}}$.

(iii) Obtain the variance of the sample around the mean spectrum F_{λ}^{var} . Note that it is actually the application of Eq. 3, which requires $F_{\lambda}^{\text{mean}}$.

(iv) Obtain the final SBF galaxy spectrum by dividing F_{λ}^{var} by $F_{\lambda}^{\text{mean}}$.

This procedure requires that the noise, i.e. the contribu-

tion to the fluctuation that is not linked to the stellar population itself, is sufficiently low such that it does not overwhelm the SBF signal. IFU data has the advantage that it provides the evaluation of the error in the flux at each position and wavelength during data processing. From the theoretical spectra we find that the SBF luminosities range from about, 1×10^{33} to 1×10^{29} erg/s/Å from young to old ages, respectively. Since the fluctuations diminish with distance, we might be able to measure deviations of about 1×10^{-17} (1×10^{-21}) erg/s/Å/cm⁻² for a young (old) stellar population for a distance of 1 Mpc. These fluctuations would be 100 times dimmer at 10 Mpc, and the variance associated with the IFU data should be lower than, at least, 10 times the SBF fluctuation value. Depending on the observations this method might not be a reliable option with respect to that making use of the FT (as in Mitzkus et al. 2018).

A second procedure is to obtain the SBF spectrum from galaxy spectroscopic surveys. In this case the requirement is that all the selected galaxies share very similar spectra as a result of their evolutionary properties. At a given redshift, the spectral properties of ETGs are mostly driven by galaxy mass (traced by their central velocity dispersion measurement). This allows us to obtain a common mean or a stacked spectrum. In this case the inferences obtained from the analysis of the SBF do not refer to any particular galaxy (as well as the standard SBF does not refer to any particular pixel), but to the characteristics of the overall sample. This type of analysis cannot be performed using the PSF-based method, since there is no common PSF, but it requires an exquisite treatment of the observational errors and biases in the employed data.

We further emphasize that these two approaches are based on the assumption that the ensemble of observational spectra share similar relevant stellar population properties, otherwise the derived properties from the SBF might be driven by the varying populations. Another important caveat to consider here is that in this simple approach for obtaining the observational SBF spectrum we do not take into account any potential contributions to the variance from instrumental noise, the presence of globular clusters, foreground stars or background galaxies. Fortunately, the instrumental noise can be remedied to a great extent by employing high quality galaxy spectra with relatively high signal-to-noise.

Finally, we would like to make the point that in order to fit the observational SBF spectra, or in using them as a metrics in full spectral fitting of mean spectra, an appropriate methodology has to be developed. In fact we have shown in this work the very peculiar characteristics of the SBF spectra in comparison to the mean spectra. Specifically, the SBF spectra of SSPs cannot be combined directly to obtain the corresponding SBF spectrum of a stellar population characterized by a given SFH. Rather, the mean and the variance spectra must be combined separately, so that we keep the properties of the latter in the resulting stellar population. Such characteristics prevents the use of current algorithms that aim at inferring relevant stellar population properties and SFHs using a full spectrum fitting approach. These limitations were discussed by Mitzkus et al. (2018), who showed that the only way to handle an observational SBF spectrum is by using it *a posteriori* constraint over the best fitted solution. However, neither the theoretical nor the observa-

Table A1. Maximum and minimum offsets derived for each metallicity bin for the Galex NUV and the Johnson-Cousin broad band filters. These offsets are meant to be applied to the values obtained with Eq. 8 to correct the spectroscopic fluctuation magnitudes from non full correlation effects within the filter passband. These values were derived from varying the input set of isochrones (Padova00 and BaSTI) over the old age regime (4–13 Gyr). The absolute minimum and maximum offsets obtained among all the metallicity bins covered by our models are highlighted in bold face.

| Z | NUV _{GALEX} | | U | | B2 | | B3 | | V | | R _{Cousin} | |
|--------|----------------------|---------------|---------------|---------------|---------------|---------------|---------------|---------------|---------------|---------------|---------------------|---------------|
| | max. | min. | max. | min. | max. | min. | max. | min. | max. | min. | max. | min. |
| 0.0001 | -0.069 | -0.011 | -0.025 | -0.009 | -0.035 | -0.014 | -0.037 | -0.015 | -0.008 | -0.002 | -0.017 | -0.001 |
| 0.0003 | -0.073 | -0.009 | -0.028 | -0.009 | -0.041 | -0.014 | -0.043 | -0.014 | -0.005 | -0.002 | -0.014 | -0.001 |
| 0.0004 | -0.075 | -0.009 | -0.031 | -0.010 | -0.047 | -0.014 | -0.049 | -0.014 | -0.005 | -0.002 | -0.012 | -0.001 |
| 0.0006 | -0.074 | -0.008 | -0.037 | -0.012 | -0.058 | -0.016 | -0.061 | -0.017 | -0.005 | -0.002 | -0.008 | -0.001 |
| 0.0010 | -0.072 | -0.008 | -0.038 | -0.014 | -0.065 | -0.021 | -0.069 | -0.023 | -0.005 | -0.002 | -0.008 | -0.002 |
| 0.0020 | -0.080 | -0.011 | -0.042 | -0.018 | -0.082 | -0.027 | -0.086 | -0.029 | -0.008 | -0.004 | -0.019 | -0.010 |
| 0.0040 | -0.095 | -0.029 | -0.031 | -0.021 | -0.045 | -0.033 | -0.048 | -0.035 | -0.009 | -0.006 | -0.050 | -0.025 |
| 0.0080 | -0.098 | -0.034 | -0.028 | -0.019 | -0.040 | -0.030 | -0.043 | -0.032 | -0.014 | -0.008 | -0.092 | -0.060 |
| 0.0100 | -0.097 | -0.023 | -0.031 | -0.017 | -0.040 | -0.028 | -0.042 | -0.030 | -0.015 | -0.008 | -0.094 | -0.066 |
| 0.0190 | -0.041 | -0.010 | -0.040 | -0.026 | -0.039 | -0.027 | -0.042 | -0.028 | -0.019 | -0.014 | -0.102 | -0.066 |
| 0.0240 | -0.045 | -0.009 | -0.039 | -0.025 | -0.038 | -0.024 | -0.040 | -0.026 | -0.018 | -0.014 | -0.098 | -0.071 |
| 0.0300 | -0.025 | -0.004 | -0.058 | -0.029 | -0.044 | -0.021 | -0.047 | -0.022 | -0.016 | -0.013 | -0.093 | -0.061 |
| 0.0400 | -0.020 | -0.004 | -0.056 | -0.027 | -0.041 | -0.015 | -0.044 | -0.016 | -0.015 | -0.011 | -0.084 | -0.060 |

| Z | I _{Cousin} | | J _{Johnson} | | J _{Bessell} | | J _{2MASS} | | H | | K | |
|--------|---------------------|--------------|----------------------|--------------|----------------------|--------------|--------------------|--------------|---------------|--------------|---------------|--------------|
| | max. | min. | max. | min. | max. | min. | max. | min. | max. | min. | max. | min. |
| 0.0001 | -0.011 | 0.000 | -0.009 | 0.000 | -0.008 | 0.000 | -0.007 | 0.000 | -0.006 | 0.000 | -0.007 | 0.000 |
| 0.0003 | -0.008 | 0.000 | -0.003 | 0.000 | -0.002 | 0.000 | -0.001 | 0.000 | -0.002 | 0.000 | -0.002 | 0.000 |
| 0.0004 | -0.007 | 0.000 | -0.003 | -0.001 | -0.002 | 0.000 | -0.002 | 0.000 | -0.002 | 0.000 | -0.002 | 0.000 |
| 0.0006 | -0.007 | 0.000 | -0.004 | -0.001 | -0.002 | 0.000 | -0.002 | 0.000 | -0.002 | 0.000 | -0.002 | 0.000 |
| 0.0010 | -0.007 | -0.001 | -0.004 | -0.002 | -0.002 | 0.000 | -0.002 | 0.000 | -0.002 | 0.000 | -0.003 | 0.000 |
| 0.0020 | -0.019 | -0.004 | -0.003 | -0.001 | -0.002 | 0.000 | -0.001 | 0.000 | -0.002 | 0.000 | -0.004 | 0.000 |
| 0.0040 | -0.036 | -0.010 | -0.002 | 0.000 | -0.001 | 0.000 | -0.001 | 0.000 | -0.002 | -0.001 | -0.003 | 0.000 |
| 0.0080 | -0.048 | -0.029 | -0.002 | 0.000 | -0.001 | 0.000 | -0.001 | 0.000 | -0.003 | -0.001 | -0.006 | -0.001 |
| 0.0100 | -0.051 | -0.035 | -0.002 | 0.000 | -0.001 | 0.000 | -0.001 | 0.000 | -0.003 | -0.001 | -0.007 | -0.001 |
| 0.0190 | -0.080 | -0.051 | -0.004 | -0.001 | -0.001 | 0.000 | -0.001 | 0.000 | -0.004 | -0.001 | -0.010 | -0.003 |
| 0.0240 | -0.084 | -0.058 | -0.004 | -0.001 | -0.001 | 0.000 | -0.001 | 0.000 | -0.004 | -0.001 | -0.011 | -0.004 |
| 0.0300 | -0.088 | -0.068 | -0.004 | -0.002 | -0.002 | -0.001 | -0.002 | 0.000 | -0.005 | -0.002 | -0.012 | -0.004 |
| 0.0400 | -0.095 | -0.071 | -0.005 | -0.003 | -0.002 | -0.001 | -0.002 | 0.000 | -0.004 | -0.002 | -0.014 | -0.007 |

tional SBF spectra have been properly taken into account in full spectral fitting algorithms. The inclusion of the observational SBF spectrum in spectral fitting should in principle improve our ability to derive the best matching stellar population model. Current fitting approaches simply choose the model that minimizes the χ^2 , i.e. the one that provides the smallest residuals, irrespective of whether these come from observational errors or not. The time is ripe for performing a detailed study to determine an optimal methodology for incorporating SBF spectra in the analysis of stellar populations. Such improvements potentially represent a major advantage for the interpretation of incoming data of nearby stellar populations taken with the new generation of large telescopes, which provide enhanced spatial resolutions. It is our intention to address this methodology elsewhere.

Table A2. As Table A1 but for SDSS filter responses.

| Z | u | | g | | r | | i | | z | |
|--------|---------------|---------------|---------------|---------------|---------------|--------------|---------------|--------------|---------------|--------------|
| | max. | min. | max. | min. | max. | min. | max. | min. | max. | min. |
| 0.0001 | -0.028 | -0.011 | -0.025 | -0.010 | -0.008 | 0.000 | -0.009 | 0.000 | -0.009 | 0.000 |
| 0.0003 | -0.029 | -0.012 | -0.028 | -0.009 | -0.004 | 0.000 | -0.006 | 0.000 | -0.005 | 0.000 |
| 0.0004 | -0.030 | -0.012 | -0.031 | -0.009 | -0.004 | 0.000 | -0.007 | 0.000 | -0.005 | -0.001 |
| 0.0006 | -0.033 | -0.013 | -0.036 | -0.010 | -0.002 | -0.001 | -0.008 | 0.000 | -0.005 | -0.001 |
| 0.0010 | -0.035 | -0.014 | -0.042 | -0.013 | -0.003 | -0.001 | -0.009 | 0.000 | -0.005 | -0.001 |
| 0.0020 | -0.035 | -0.016 | -0.056 | -0.017 | -0.006 | -0.003 | -0.026 | -0.006 | -0.006 | -0.001 |
| 0.0040 | -0.025 | -0.015 | -0.029 | -0.021 | -0.009 | -0.006 | -0.048 | -0.017 | -0.016 | -0.001 |
| 0.0080 | -0.023 | -0.015 | -0.028 | -0.021 | -0.017 | -0.008 | -0.082 | -0.061 | -0.022 | -0.006 |
| 0.0100 | -0.025 | -0.013 | -0.029 | -0.021 | -0.016 | -0.009 | -0.089 | -0.066 | -0.024 | -0.010 |
| 0.0190 | -0.031 | -0.021 | -0.032 | -0.023 | -0.014 | -0.010 | -0.124 | -0.074 | -0.059 | -0.041 |
| 0.0240 | -0.030 | -0.020 | -0.030 | -0.022 | -0.013 | -0.010 | -0.122 | -0.082 | -0.063 | -0.048 |
| 0.0300 | -0.049 | -0.025 | -0.031 | -0.019 | -0.011 | -0.009 | -0.119 | -0.081 | -0.070 | -0.052 |
| 0.0400 | -0.049 | -0.024 | -0.029 | -0.013 | -0.010 | -0.007 | -0.114 | -0.080 | -0.074 | -0.057 |

| Z | u' | | g' | | r' | | i' | | z' | |
|--------|---------------|---------------|---------------|---------------|---------------|--------------|---------------|--------------|---------------|--------------|
| | max. | min. | max. | min. | max. | min. | max. | min. | max. | min. |
| 0.0001 | -0.039 | -0.016 | -0.029 | -0.011 | -0.009 | 0.000 | -0.011 | 0.000 | -0.009 | 0.000 |
| 0.0003 | -0.040 | -0.016 | -0.032 | -0.010 | -0.006 | 0.000 | -0.008 | 0.000 | -0.003 | 0.000 |
| 0.0004 | -0.041 | -0.017 | -0.035 | -0.010 | -0.005 | 0.000 | -0.009 | 0.000 | -0.003 | 0.000 |
| 0.0006 | -0.043 | -0.018 | -0.041 | -0.012 | -0.003 | -0.001 | -0.010 | 0.000 | -0.004 | 0.000 |
| 0.0010 | -0.043 | -0.018 | -0.047 | -0.014 | -0.004 | -0.001 | -0.010 | 0.000 | -0.003 | -0.001 |
| 0.0020 | -0.041 | -0.020 | -0.064 | -0.019 | -0.008 | -0.003 | -0.026 | -0.005 | -0.003 | -0.001 |
| 0.0040 | -0.029 | -0.018 | -0.034 | -0.025 | -0.014 | -0.009 | -0.046 | -0.016 | -0.009 | -0.001 |
| 0.0080 | -0.027 | -0.018 | -0.032 | -0.025 | -0.025 | -0.012 | -0.069 | -0.051 | -0.013 | -0.004 |
| 0.0100 | -0.029 | -0.017 | -0.032 | -0.025 | -0.024 | -0.013 | -0.075 | -0.055 | -0.014 | -0.006 |
| 0.0190 | -0.041 | -0.029 | -0.035 | -0.026 | -0.019 | -0.015 | -0.104 | -0.066 | -0.037 | -0.027 |
| 0.0240 | -0.040 | -0.029 | -0.033 | -0.024 | -0.018 | -0.015 | -0.104 | -0.073 | -0.038 | -0.029 |
| 0.0300 | -0.075 | -0.036 | -0.033 | -0.020 | -0.016 | -0.012 | -0.104 | -0.076 | -0.043 | -0.031 |
| 0.0400 | -0.075 | -0.036 | -0.030 | -0.014 | -0.013 | -0.011 | -0.103 | -0.077 | -0.043 | -0.034 |

Table A3. As Table A1 but for HST filter responses.

| Z | F439W | | F555W | | FW675W | | F814W | |
|--------|---------------|---------------|---------------|---------------|---------------|--------------|---------------|--------------|
| | max. | min. | max. | min. | max. | min. | max. | min. |
| 0.0001 | -0.018 | -0.007 | -0.014 | -0.004 | -0.009 | 0.000 | -0.017 | 0.000 |
| 0.0003 | -0.021 | -0.007 | -0.013 | -0.004 | -0.004 | 0.000 | -0.014 | 0.000 |
| 0.0004 | -0.025 | -0.007 | -0.012 | -0.004 | -0.005 | 0.000 | -0.014 | 0.000 |
| 0.0006 | -0.032 | -0.008 | -0.012 | -0.004 | -0.005 | 0.000 | -0.015 | 0.000 |
| 0.0010 | -0.036 | -0.012 | -0.013 | -0.005 | -0.005 | 0.000 | -0.016 | -0.001 |
| 0.0020 | -0.044 | -0.016 | -0.019 | -0.008 | -0.012 | -0.004 | -0.034 | -0.007 |
| 0.0040 | -0.029 | -0.021 | -0.015 | -0.012 | -0.023 | -0.011 | -0.059 | -0.020 |
| 0.0080 | -0.025 | -0.019 | -0.020 | -0.014 | -0.047 | -0.023 | -0.080 | -0.056 |
| 0.0100 | -0.026 | -0.018 | -0.021 | -0.014 | -0.046 | -0.026 | -0.087 | -0.065 |
| 0.0190 | -0.027 | -0.019 | -0.022 | -0.017 | -0.042 | -0.029 | -0.129 | -0.091 |
| 0.0240 | -0.026 | -0.018 | -0.020 | -0.017 | -0.039 | -0.030 | -0.137 | -0.102 |
| 0.0300 | -0.038 | -0.015 | -0.019 | -0.014 | -0.036 | -0.025 | -0.147 | -0.116 |
| 0.0400 | -0.036 | -0.011 | -0.016 | -0.012 | -0.030 | -0.024 | -0.164 | -0.123 |
| Z | WFC475 | | WFC606 | | WFC814 | | | |
| | max. | min. | max. | min. | max. | min. | | |
| 0.0001 | -0.025 | -0.000 | -0.018 | -0.003 | -0.017 | 0.000 | | |
| 0.0003 | -0.027 | -0.009 | -0.013 | -0.003 | -0.013 | 0.000 | | |
| 0.0004 | -0.030 | -0.009 | -0.011 | -0.003 | -0.014 | -0.001 | | |
| 0.0006 | -0.034 | -0.010 | -0.009 | -0.003 | -0.014 | -0.001 | | |
| 0.0010 | -0.039 | -0.012 | -0.009 | -0.005 | -0.014 | -0.001 | | |
| 0.0020 | -0.053 | -0.016 | -0.016 | -0.008 | -0.029 | -0.006 | | |
| 0.0040 | -0.028 | -0.021 | -0.021 | -0.016 | -0.054 | -0.017 | | |
| 0.0080 | -0.028 | -0.021 | -0.032 | -0.020 | -0.071 | -0.046 | | |
| 0.0100 | -0.029 | -0.022 | -0.031 | -0.020 | -0.074 | -0.055 | | |
| 0.0190 | -0.032 | -0.024 | -0.026 | -0.021 | -0.114 | -0.081 | | |
| 0.0240 | -0.030 | -0.022 | -0.024 | -0.020 | -0.123 | -0.091 | | |
| 0.0300 | -0.029 | -0.019 | -0.022 | -0.016 | -0.133 | -0.107 | | |
| 0.0400 | -0.027 | -0.014 | -0.019 | -0.016 | -0.151 | -0.113 | | |